

See discussions, stats, and author profiles for this publication at: <https://www.researchgate.net/publication/290591255>

Constitutive modeling of sand: Formulation of a new plasticity approach

ARTICLE *in* SOIL DYNAMICS AND EARTHQUAKE ENGINEERING · MARCH 2016

Impact Factor: 1.22 · DOI: 10.1016/j.soildyn.2015.12.014

READS

9

2 AUTHORS:



[Panagiota Tasiopoulou](#)

National Technical University of Athens

25 PUBLICATIONS 46 CITATIONS

[SEE PROFILE](#)

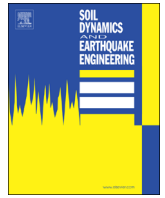


[Nikos Gerolymos](#)

National Technical University of Athens

72 PUBLICATIONS 534 CITATIONS

[SEE PROFILE](#)



Constitutive modeling of sand: Formulation of a new plasticity approach

Panagiota Tasiopoulou, Nikos Gerolymos*

National Technical University of Athens, Greece



ARTICLE INFO

Article history:

Received 17 July 2015

Received in revised form

17 December 2015

Accepted 22 December 2015

Keywords:

Constitutive soil modeling

Sand

Monotonic and cyclic loading

Bouc–Wen hysteresis

Plasticity

Liquefaction

Critical state

Stress path

ABSTRACT

A constitutive model for sand is derived based on a new theoretical framework that combines features of perfect elastoplasticity and smooth hysteresis. It resembles a bounding surface model with vanished elastic region, but with considerable modifications in that the plastic modulus is not explicitly defined, and the mapping rule is Bouc–Wen motivated and works equally well in monotonic as in stress-reversal loading. Among the proposed features, are: (a) critical state compatibility not only for monotonic but also for cyclic loading, and (b) novel plastic flow rule accounting for anisotropic distribution of the dilatancy strain ratio, d , to the normal plastic strain increments. The capability of the model in capturing complex aspects of sand behavior (e.g. cyclic mobility, static liquefaction, densification) is demonstrated through illustrative paradigms with emphasis on the physical meaning of each key-model parameter and comparisons with experimental data.

© 2015 Elsevier Ltd. All rights reserved.

1. Introduction

The behavioral diversity of sand for different loadings (drained/undrained, monotonic/cyclic), initial stresses and fabric conditions, renders its modeling a difficult and challenging task. The suitability of the used constitutive model is evaluated by its capability to capture the trends across all these conditions without recalibration of its parameters for each specific case, but also by its simplicity. Too many parameters might increase the versatility of the model at the risk, however, of losing its physical meaning.

In the last three decades, many constitutive models for sand have been proposed, each with varying degree of accuracy and applicability. The most promising ones are plasticity-based that incorporate the effective stress and critical state concepts (e.g.: [5,7,9,14,22,27–31,36]), though recently developed hypoplastic models have shown remarkable predictive capability (e.g. [19,23]). In this paper, a constitutive model for sand is presented based on a new plasticity framework that joins together features from perfect elastoplasticity and Bouc–Wen type of hysteresis. The motivation is to develop an alternative plasticity formulation that exhibits critical state compatibility for both monotonic and cyclic loading

and uniqueness of its parameters for a given type of sand, irrespective of loading conditions.

The model, designated as Ta-Ger sand model, is based on a reformulation of perfect elastoplasticity by introducing a hardening law inspired from smooth hysteretic modeling. The objective of smooth hysteretic models is to provide a continuous function between an input (displacement, strain etc.) and an output (force, stress etc.) for systems exhibiting hysteresis. In the areas of smart structures and civil engineering, the main class of smooth hysteresis models is represented by the so-called Bouc–Wen model, originally proposed by Bouc [4] and subsequently extended by Wen [41] and used in random vibration analysis of inelastic systems. Since then, modified or extended versions of this model have been extensively applied in modeling structural (e.g. [17,34,39]) and soil behavior (e.g. [15,16,18]). In the present study, the smooth-hysteresis concept is combined with perfect elastoplasticity, resulting in a definite and continuous expression of an elastoplastic matrix, connecting the strain (input) with the stress increment (output). The motivation behind this new plasticity approach, which couples the perfect elastoplasticity with pre-failure smooth hysteresis, is the formulation of an explicit elastoplastic matrix with the following advantages when compared to classical elastoplasticity: (i) the explicit definition of the plastic modulus and the loading index is not necessary, and (ii) no inversion of the strain–stress increment equation is required, since the current plasticity approach is formulated from the start in stress–strain increment terms. Therefore, stress point algorithms

* Corresponding author. Tel.: +30 210 7724211; fax: +30 210 7722405.

E-mail addresses: ptasiopoulou@gmail.com (P. Tasiopoulou), gerolymos@gmail.com (N. Gerolymos).

and iterative procedures associated with the prediction of the loading index and the stress increment, are avoided, rendering the numerical implementation a simpler and more efficient task.

The framework of the new plasticity approach is then used for developing a constitutive model for sand. The developed constitutive formulation can be regarded as a single-surface model with vanished elastic region and the distinguished characteristic of an explicitly defined plastic matrix instead of a plastic modulus. Salient features of the proposed plasticity approach are: (i) a new plastic flow rule which is based on a revision of Rowe's dilatancy theory (1962) to account for anisotropic distribution of the dilatancy to the normal plastic strain increments as well as densification due to cyclic loading, (ii) a mapping rule incorporated in the elastoplastic matrix and a load reversal criterion based on the sign of the first order work, and (iii) a new formulation for the critical state concept that introduces two "state" parameters. The first being the cumulative incremental deviatoric strain, controlling the transition from the initial to the critical state strength ratio and the second one being the relative dilatancy index, I_R , as originally proposed by Bolton [3], associated with the critical state line in D_r-p space. The main advantage against the traditional formulation involving only the state parameter Ψ [1,27], is critical state consistency for cyclic loading and avoidance of early shear locking in cyclic undrained response (as observed in [9]).

In the following sections, the reader is initially introduced to the proposed plasticity approach which is a general platform that can be used for a macroscopic constitutive description of a wide range of hysteretic materials when combined with an appropriate failure surface and plastic flow rule. The development of the new plasticity framework is presented step by step resulting in the formulation of an elastoplastic matrix that involves two key-variables, ζ and n . Without loss of generality, the role of each key-variable in the current plasticity framework is exemplary

demonstrated by using the Drucker–Prager failure surface. The presented plasticity platform, serves as the basis for developing an integrated constitutive model for sand. The formulation of the constitutive model is described in detail, emphasizing the effect of the key-variables and state parameters on the behavior of sand. Finally, the model is shown to be capable of reproducing complicated experimental behavior with satisfactory engineering accuracy, however, its complete calibration is beyond the scope of this paper.

2. Plasticity concept: combining perfect plasticity with Bouc-Wen type hysteresis

The governing equations of a typical elastoplastic formulation with no hardening (elastic/perfectly-plastic behavior), in generalized stress space, are revisited. For reasons of simplicity and convenience, the equations are given in the form of matrices instead of tensors in this section. The incremental total strain, $\{de\}$, is decomposed into its elastic and plastic counterparts $\{de^e\}$ and $\{de^p\}$:

$$\{de\} = \{de^e\} + \{de^p\} \tag{1}$$

The plastic strain increment is obtained from the flow rule:

$$\{de^p\} = \langle l \rangle \frac{\partial g(\{\sigma\})}{\partial \{\sigma\}} \tag{2}$$

Eq. (2) applies normality of the plastic strain increment to a plastic potential function g . l is the scalar-valued stress-dependent multiplier, designated as the loading index. Substituting Eq. (2) into Eq. (1) and applying the theory of elasticity, $\{d\sigma\} = \{E^e\}\{de^e\}$, $\{E^e\}$ being the linear elastic matrix, the following stress-strain relationship is

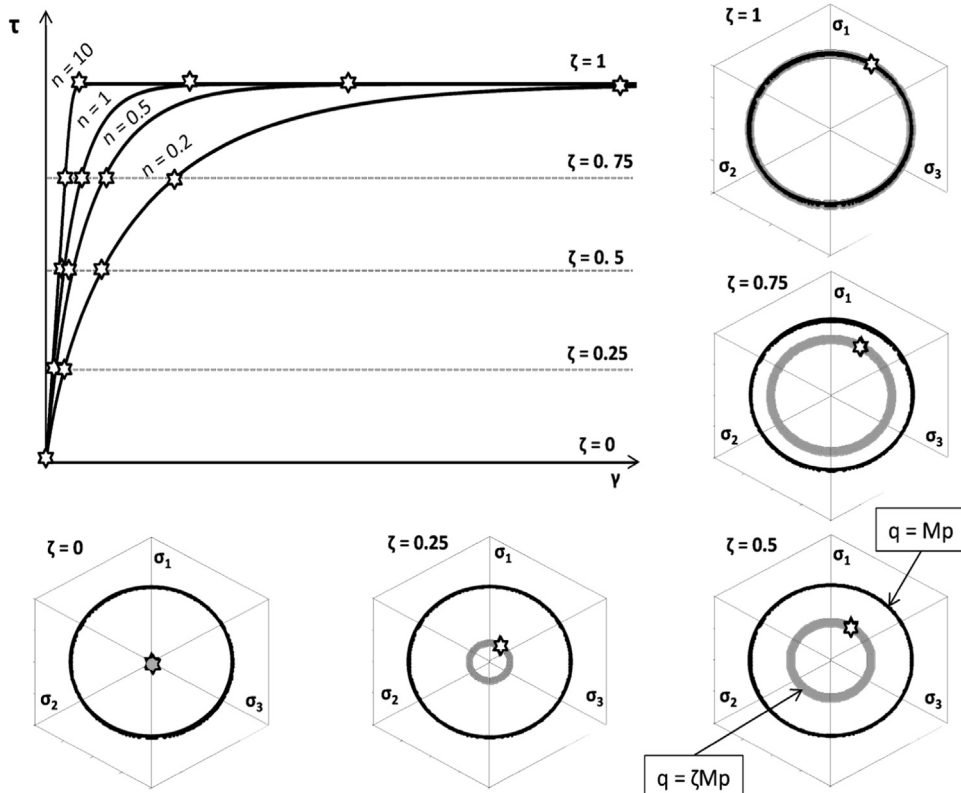


Fig. 1. Evolution of parameter ζ during loading and influence of hardening exponent n on the predicted response, in case of a Drucker–Prager failure criterion. The star symbols characterize the current stress states. The π -plane plots correspond to $n=1$.

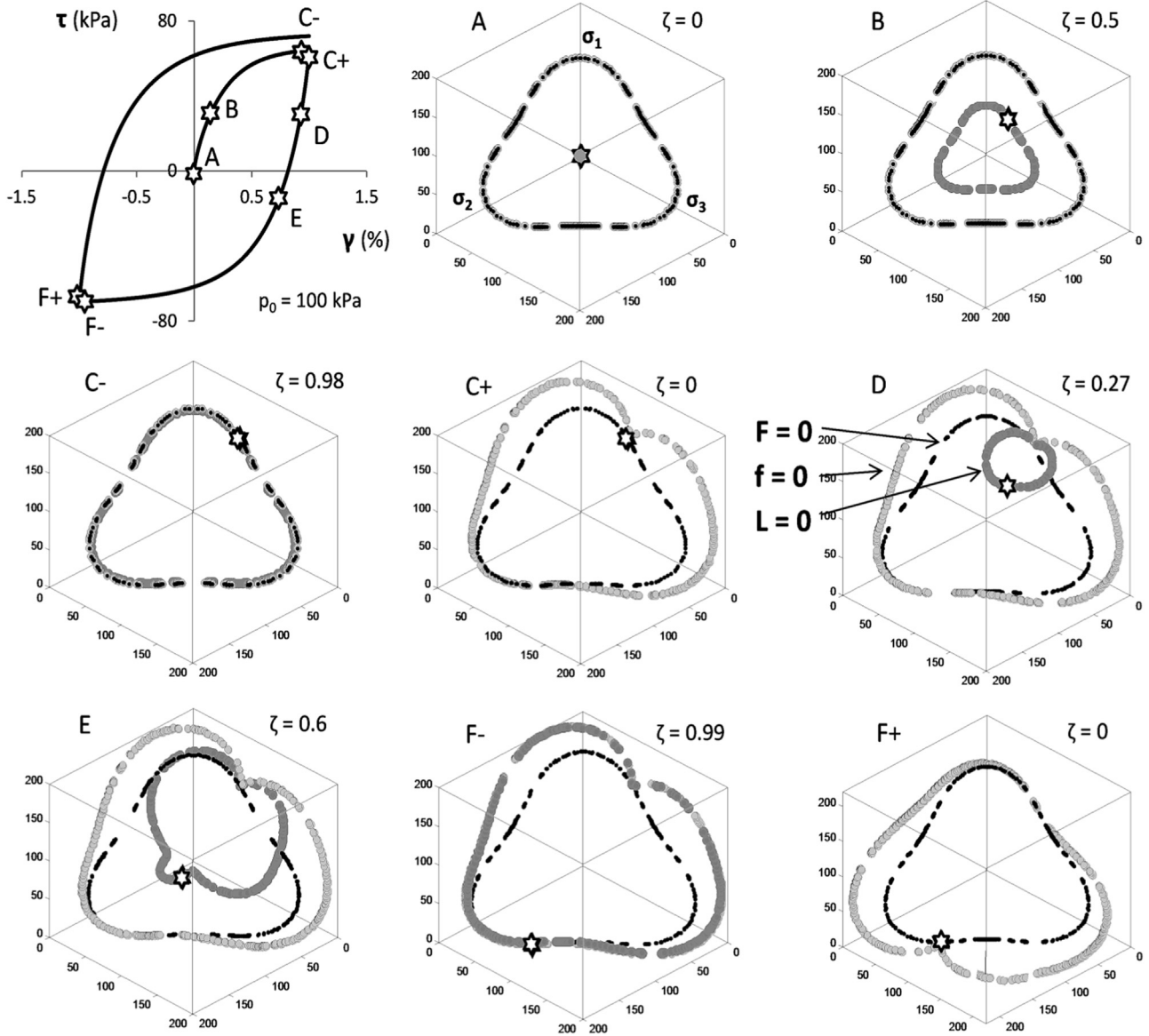


Fig. 2. Evolution of loading, $L=0$, bounding, $f=0$, and target failure, $F=0$, surface, illustrated in π -plane graphs, for a cyclic simple shear test with constant mean effective stress. The star symbols characterize the current stress state.

obtained:

$$\{d\sigma\} = \{E^e\} \left(\{d\epsilon\} - \langle l \rangle \frac{\partial g(\{\sigma\})}{\partial \{\sigma\}} \right) \quad (3)$$

For a perfectly plastic material, the yield surface, f , is fixed in stress space and thus not functionally dependent on any other state variable than stress. Plastic deformation occurs only when the stress point reaches and lies on the failure surface. This postulate is stated by the following consistency equation:

$$df(\{\sigma\}) = 0 \Rightarrow \left(\frac{\partial f}{\partial \{\sigma\}} \right)^T \{d\sigma\} = 0 \quad (4)$$

Combining Eqs. (3) and (4), one can obtain both the definition of the loading index, l , and the elastoplastic stress–strain relationship, in respect:

$$\langle l \rangle = \frac{\left(\frac{\partial f}{\partial \{\sigma\}} \right)^T \{E^e\}}{\left(\frac{\partial f}{\partial \{\sigma\}} \right)^T \{E^e\} \left(\frac{\partial g}{\partial \{\sigma\}} \right)} \{d\epsilon\} \quad (5)$$

$$\{d\sigma\} = \{E^e\} \left[\langle l \rangle - \frac{\left(\frac{\partial g}{\partial \{\sigma\}} \right) \left(\frac{\partial f}{\partial \{\sigma\}} \right)^T \{E^e\}}{\left(\frac{\partial f}{\partial \{\sigma\}} \right)^T \{E^e\} \left(\frac{\partial g}{\partial \{\sigma\}} \right)} \right] \{d\epsilon\} \quad (6)$$

Then, the elastic-perfectly-plastic matrix is derived:

$$\{E^{ep}\} = \{E^e\} \left[\langle l \rangle - \frac{\{\Phi_g\} \{\Phi_f\}^T \{E^e\}}{\{\Phi_f\}^T \{E^e\} \{\Phi_g\}} \right] \quad (7)$$

where $\{\Phi_f\}$ and $\{\Phi_g\}$ account for the gradients of yield surface and plastic potential surface, respectively:

$$\{\Phi_f\} = \frac{\partial f}{\partial \{\sigma\}}, \quad \{\Phi_g\} = \frac{\partial g}{\partial \{\sigma\}} \quad (8)$$

Thus far, it is clear that no kind of hardening response can be accommodated by the current formulation, allowing only for elastic/perfectly-plastic predictions. The intention is to attribute hardening/softening characteristics to the elastic-perfectly-plastic nature of Eq. (7), while deviating from the classical plasticity framework which involves the introduction of a plastic modulus, K_p ,

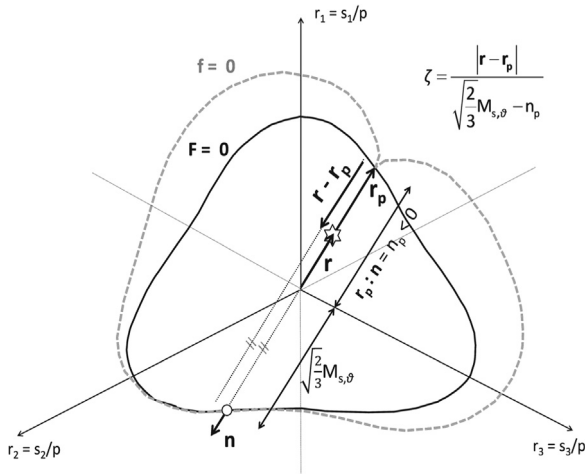


Fig. 3. Definition of parameter ζ upon first loading reversal (point D of Fig. 2) for a cyclic simple shear test with constant mean effective stress. The star symbol characterizes the current stress state, while the circle corresponds to “image” stress point.

in the denominator of Eq. (7), according to:

$$\{E_h^{ep}\} = \{E^e\} \left[\{I\} - \frac{\{\Phi_g\}\{\Phi_f\}^T\{E^e\}}{K_p + \{\Phi_f\}^T\{E^e\}\{\Phi_g\}} \right] \quad (9)$$

To this end, an appropriate plastic matrix $\{H\}$ is directly inserted in Eq. (7) by multiplying the right-hand side term inside the parentheses:

$$\{E_h^{ep}\} = \{E^e\} \left[\{I\} - \frac{\{\Phi_g\}\{\Phi_f\}^T\{E^e\}\{H\}}{\{\Phi_f\}^T\{E^e\}\{\Phi_g\}} \right] \quad (10)$$

Our goal is to provide a simpler but equally efficient scheme with higher versatility. Therefore, the role assigned to the matrix $\{H\}$ is threefold: (i) it offers a gradual and smooth (“hardening-type”) transition from the elastic to perfectly plastic response in order to capture pre-failure nonlinearity and the coupling between elastic and plastic counterparts composing the total strain increment, (ii) it provides an appropriate loading/unloading/reloading mapping rule by tracking the distance from the ultimate perfectly plastic state as defined by the failure surface, which herein, serves as a bounding surface in the sense that it indicates the ultimate

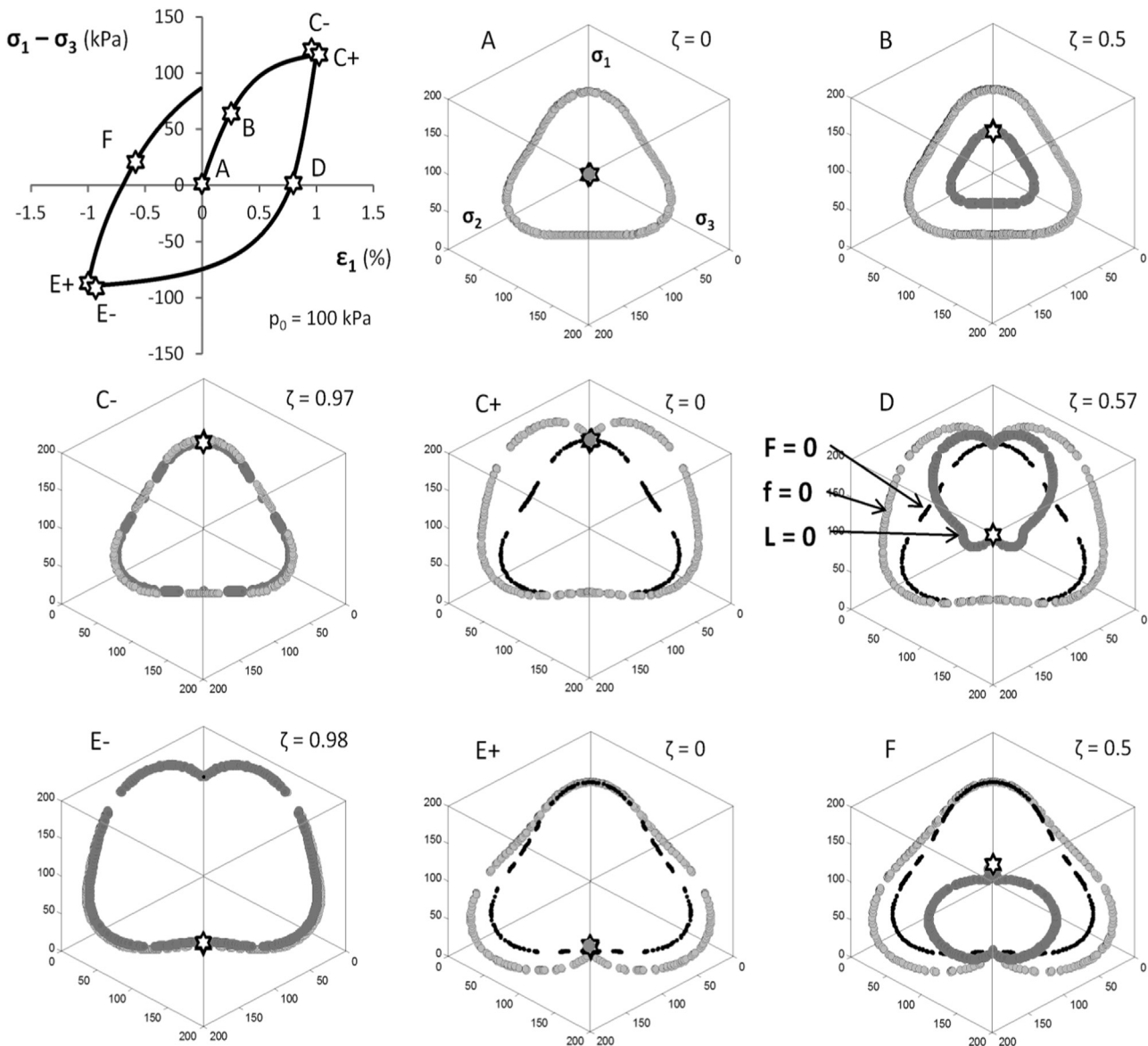


Fig. 4. Evolution of loading, $L=0$, bounding, $f=0$, and target failure surface, $F=0$ illustrated in π -plane graphs, for a cyclic triaxial p -constant test. The star symbols characterize the current stress states.

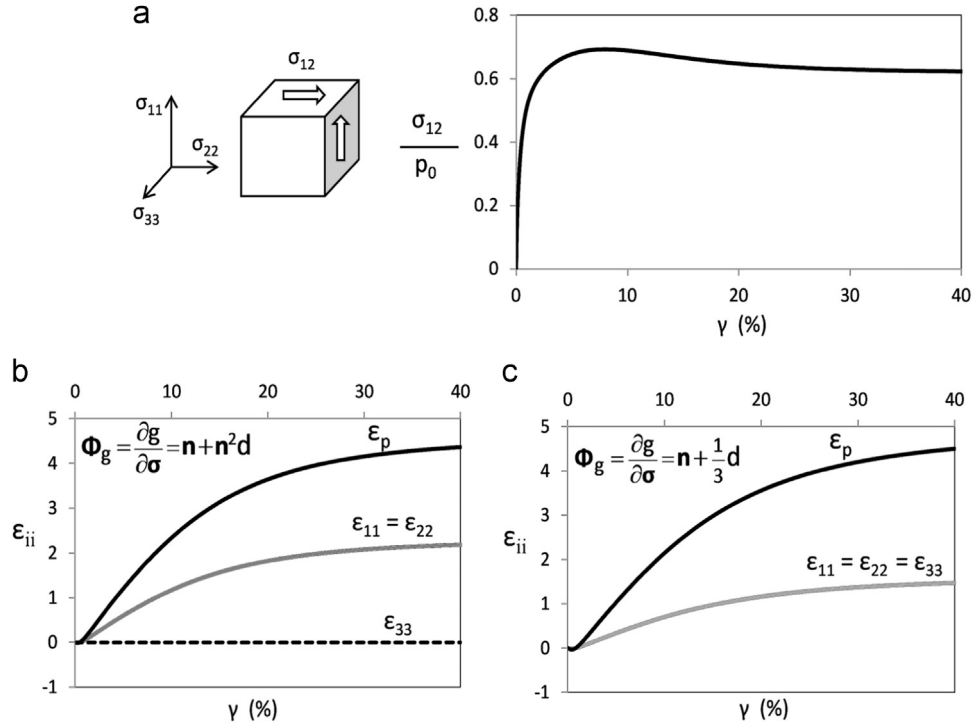


Fig. 5. Distribution/evolution of normal strain increments during a monotonic drained simple shear element test (a). Model prediction is held for both assumed gradients of plastic potential surface: (b) Eq. (33) and (c) (35).

strength which cannot be surpassed, and (iii) the values of its terms are strictly bounded within the range of [0,1]. In this line of thought, the matrix {H} acquires only diagonal terms as a function of a dimensionless parameter ζ , satisfying the second and third requirements, and a hardening exponent parameter, n , fulfilling the first postulate. Both of these parameters, considered key-variables of the current plasticity formulation, are inspired by the smooth hysteretic models of the Bouc–Wen type [15]. Matrix {H} is given as:

$$\{H\} = \zeta^n \{I\} \tag{11}$$

The components of the elastoplastic matrix of Eq. (10) can be found in the Appendix.

As it has been already stated, parameter ζ needs to be dimensionless and strictly bounded within the range [0,1]. It is obvious that ζ should obtain unit value when the stress point reaches the ultimate failure state (perfectly plastic, $f=0$), while all its intermediate values, from zero to unity, correspond to intermediate stress states. In this context, the definition of parameter ζ is derived directly from the equation of any given failure surface describing a specific material. This can be easily achieved by an appropriate reformulation of the given failure surface equation in a rational non-dimensional way, so that the final equation is equal to 1 instead of 0. In order to demonstrate an appropriate definition for parameter ζ , compatible with a specific failure surface, let us assume a material obeying a cone-type failure criterion in triaxial space, such as Drucker–Prager:

$$f = 0 \Leftrightarrow q - Mp = 0 \tag{12}$$

where q is the deviatoric stress, p is the mean effective stress and M is the failure stress ratio representing the ultimate strength, e.g. critical state. In lieu of the abovementioned requirements, a proper definition of ζ is:

$$\zeta = \frac{(q/p)}{M} \tag{13}$$

Since the stress ratio, q/p , can only obtain values within the range of [0, M], ζ is strictly bounded in the range of [0,1]. Evidently, the elastic state corresponding to $\zeta=0$, $\{H\} = \{0\}$ and $\{E^{ep}\} = \{E^e\}$, is trivialized to a single point and plastic strains develop from early on, as soon as ζ becomes greater than zero. A set of loading surfaces are created upon definition of ζ , described by the following equation:

$$q - \zeta Mp = 0 \tag{14}$$

Each stress state corresponds to a unique value of ζ resulting in a specific loading surface given by Eq. (14). Thus, each current stress point automatically lies on a surface proportional to the failure surface of Eq. (12) by the value of ζ , as illustratively depicted in Fig. 1.

Conceptually, the failure surface works similarly to a reference surface, namely a bounding surface [8], which cannot be surpassed, in the sense that for any given stress state (e.g. stress ratio, q/p) there is always an “image” stress state lying on the failure surface (e.g. stress ratio, M) so that the ratio, ζ , between the actual and “image” stress states can be measured. Specifically, for the examined case of a Drucker–Prager failure surface which forms a circle in π plane, the current stress state is equal to the radius of the current loading surface, while the “image” stress state is always equal to the radius of the failure surface (see Fig. 1).

Clearly, parameter ζ holds the role of evolution or else mapping rule. In retrospect, the plastic matrix, {H}, is dependent only on the bounding surface. Hence, the proposed plasticity approach is characterized as a single-surface model. The elastic area is trivialized to a single point at the beginning of loading, unloading and reloading, where elastic behavior is expected at least momentarily satisfying Masing rule. Hence, no yield surface is involved to define the elastic region, or rather, the yield surface diminishes to a single line for $\zeta=0$ (e.g. $q=0$ from Eq. (14) for $\zeta=0$). Needless to say that neutral loading cannot be captured in the lack of a yield surface. This fact can be advantageous upon loading reversal where

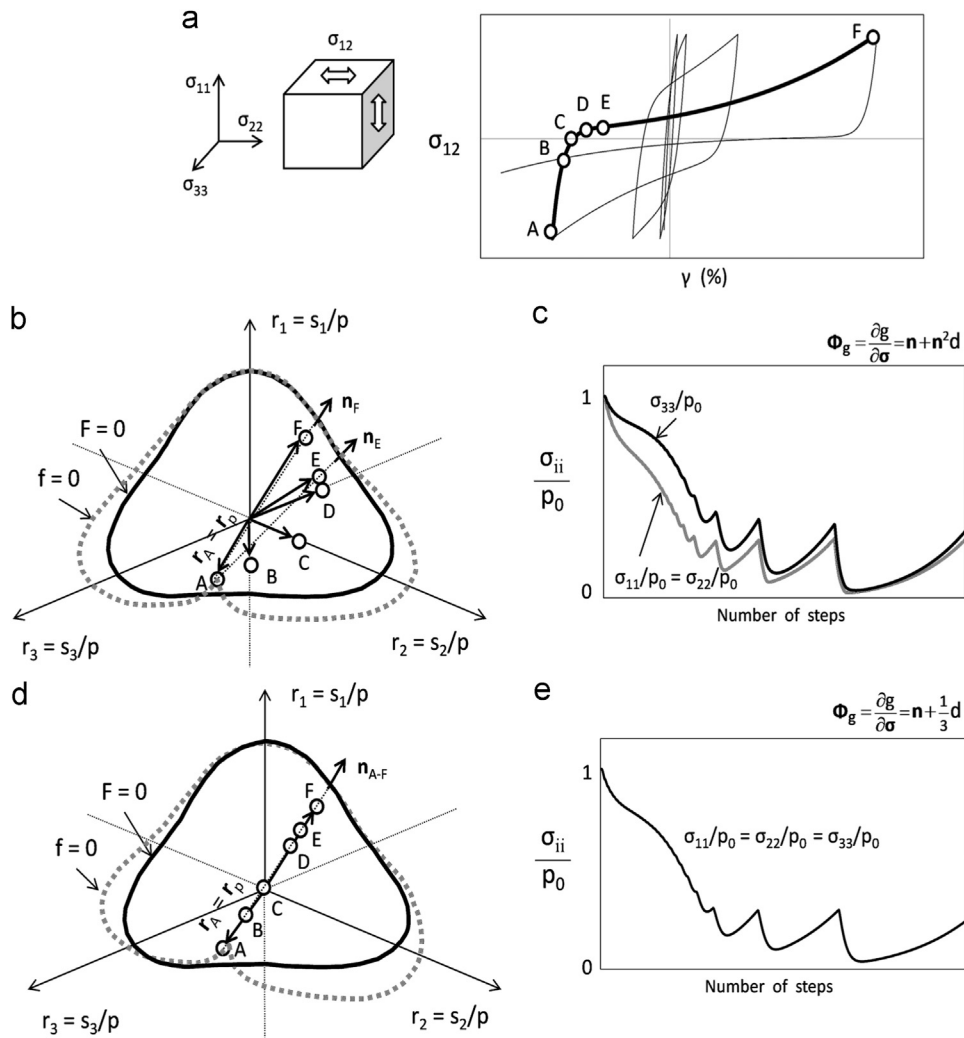


Fig. 6. (a) Stress-strain loops under cyclic shear undrained loading. (b) Stress path in π -plane using Eq. (33), (c) evolution of shear stresses using Eq. (33), (d) Stress path in π -plane using Eq. (35), and (e) evolution of shear stresses using Eq. (35).

potential unrealistic reversal of loading by neutral loading is automatically excluded; a weakness that is commonly encountered in the majority of elastoplasticity models, such as bounding surface [8], generalized-plasticity [30], multisurface ones [31] etc.

While parameter ζ tracks the actual distance of the current stress state from the failure state, exponent parameter n controls the rate of transition from elastic state to the perfectly plastic one, as characteristically demonstrated in Fig. 1 for a Drucker–Prager failure surface. Exponent n is designated as the hardening parameter in the current scheme, determining the degree of coupling between concurrent elastic and plastic strain increments during loading. As the value of n increases, the response tends to be elastic/perfectly-plastic while the elastic and plastic strain increments tend to be decoupled during loading (e.g. $n=10$), with the elastic ones occurring exclusively prior to failure (plateau) and the plastic ones developing only after failure takes place. Inversely, as the value of n decreases, the coupling between the elastic and plastic components of total strain increment increases until ultimate failure is reached, resulting in a smoother transition to failure.

3. Constitutive model for sand

The new plasticity scheme is used as a framework to develop a constitutive model for sand, attempting to capture the important

aspects of sand behavior under monotonic and cyclic loading, such as dilation/contraction, hardening/softening, densification, liquefaction and cyclic mobility. An appropriate bounding surface is proposed, which allows a unique derivation of parameter ζ for monotonic and cyclic loading by keeping memory of the last reversal stress state, while loading reversal is determined by a simple first-order work criterion. Additionally, a new set of functions is introduced for the evolution of bounding and phase transformation stress ratios in order to adopt the critical state concept.

3.1. Pre-failure parameters

The terms in matrix $\{E^e\}$, which are shown in the Appendix, are functions of the shear and bulk moduli which in turn are functions of the mean effective stress p , according to:

$$G = G_0 p_\alpha \frac{(2.97 - e)^2}{1 + e} \left(\frac{p}{p_\alpha}\right)^m, \dots \dots K = \frac{2(1 + \nu)}{3(1 - 2\nu)} G \quad (15)$$

in which, G_0 is a dimensionless material parameter, ν is the Poisson's ratio, p_α is the atmospheric pressure, e is the current void ratio, and m is a dimensionless parameter determining the rate of variation of G and K with p [20,25,32].

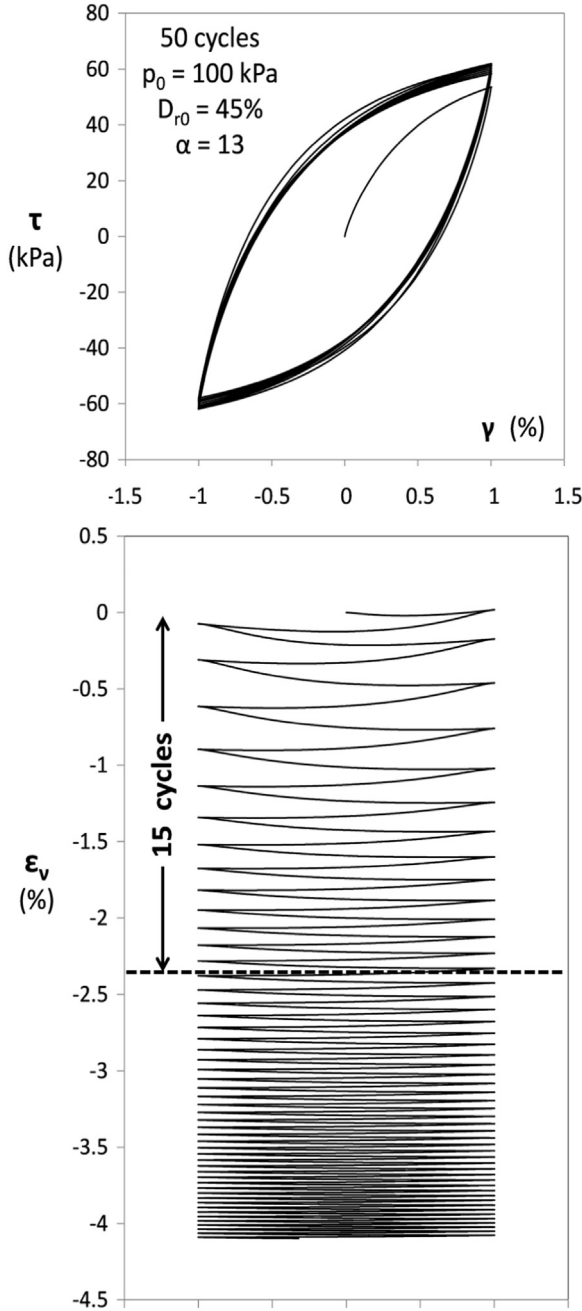


Fig. 7. Model prediction for a drained cyclic simple shear test, exhibiting densification.

3.2. Bounding surface and parameter ζ

An open-end, cone-type bounding surface is proposed as a function of the current stress state as well as the stress state at the last reversal of loading:

$$\mathbf{f} = [(\mathbf{s} - \mathbf{r}_p p) : (\mathbf{s} - \mathbf{r}_p p)]^{1/2} - \left(\sqrt{\frac{2}{3}} M_{s,\theta} - n_p \right) p = 0 \quad (16)$$

where \mathbf{s} is the second order deviatoric stress tensor and $M_{s,\theta}$ is the bounding stress ratio, determining the ultimate strength, dependent on the lode angle θ . The stress ratio tensor, \mathbf{r}_p is given by:

$$\mathbf{r}_p = \frac{\mathbf{s}_p}{p_p} = \frac{\boldsymbol{\sigma}_p - p_p \mathbf{I}}{p_p} \quad (17)$$

where $\boldsymbol{\sigma}_p$ is equal to the effective stress tensor and p_p the mean effective stress at the pivot points, once reversal of loading occurs. It

is noted that \mathbf{r}_p is comparatively equivalent to the back-stress ratio α in a conventional bounding surface model. The scalar valued stress ratio n_p is defined as the inner product of two tensors denoting the distance of the pivot stress ratio \mathbf{r}_p from the hydrostatic axis:

$$n_p = \mathbf{n} : \mathbf{r}_p \quad (18)$$

in which \mathbf{n} is a normalized stress ratio tensor, normal to f :

$$\mathbf{n} = \frac{\mathbf{s} - \mathbf{r}_p p}{[(\mathbf{s} - \mathbf{r}_p p) : (\mathbf{s} - \mathbf{r}_p p)]^{1/2}} \quad (19)$$

The properties of tensor \mathbf{n} are given by the following equations:

$$\text{tr} \mathbf{n} = n_{11} + n_{22} + n_{33} = 0 \quad (20)$$

$$\text{tr} \mathbf{n}^2 = \mathbf{n} : \mathbf{n} = n_{11}^2 + n_{22}^2 + n_{33}^2 + 2n_{12}^2 + 2n_{23}^2 + 2n_{31}^2 = 1 \quad (21)$$

Evidently, in case of monotonic loading, the bounding surface, f , returns to its common Drucker–Prager form but with Lode angle dependency:

$$F = [\mathbf{s} : \mathbf{s}]^{1/2} - \sqrt{\frac{2}{3}} M_{s,\theta} p = 0 \quad (22)$$

The evolution of its shape, once reversal occurs, is explained in Section 3.4 along with the mapping rule. Parameter ζ is defined following the same concept described in Section 2:

$$\zeta = \frac{[(\mathbf{r} - \mathbf{r}_p) : (\mathbf{r} - \mathbf{r}_p)]^{1/2}}{\sqrt{\frac{2}{3}} M_{s,\theta} - n_p} = \frac{|\mathbf{r} - \mathbf{r}_p|}{\sqrt{\frac{2}{3}} M_{s,\theta} - n_p} \quad (23)$$

in which \mathbf{r} is the current deviatoric stress ratio tensor. It is obvious that ζ obtains zero values at each point reversal, initiating elastic unloading, consistent with Masing rule. Parameter ζ ensures that the current stress state always lies on a loading surface described by:

$$L = [(\mathbf{s} - \mathbf{r}_p p) : (\mathbf{s} - \mathbf{r}_p p)]^{1/2} - \zeta \left(\sqrt{\frac{2}{3}} M_{s,\theta} - n_p \right) p = 0 \quad (24)$$

Since plasticity starts practically from $\zeta=0$, the yield surface can be derived by Eq. (24) for $\zeta=0$. The gradient to this yield surface is given by:

$$\boldsymbol{\Phi}_f = \frac{\partial f}{\partial \boldsymbol{\sigma}} = \mathbf{n} - \frac{1}{3} \mathbf{n} : \mathbf{r} \quad (25)$$

3.3. Lode angle dependency

The Lode angle is defined as:

$$\cos(3\theta) = \frac{3\sqrt{3} J_3}{2 J_2^{3/2}} \quad (26)$$

where J_2 and J_3 are the second and third deviatoric invariant, respectively. After using polynomial interpolation, $M_{s,\theta}$ can be obtained by:

$$M_{s,\theta} = \left(\frac{M_c + M_e}{2} - M_{ss} \right) \cos^2(3\theta) + \left(\frac{M_c - M_e}{2} \right) \cos(3\theta) + M_{ss} \quad (27)$$

in which M_c is the bounding stress ratio in compression, M_e in extension and M_s in simple shear. They are related to friction angle, φ , as:

$$M_c = \frac{6 \sin \varphi}{3 - \sin \varphi}; M_e = \frac{6 \sin \varphi}{3 + \sin \varphi}; M_{ss} = 2 \sin \varphi \quad (28)$$

Then, the internal model parameter χ , accounting for the Lode angle effects, is defined as:

$$\chi = \frac{M_{s,\theta}}{M_c} \quad (29)$$

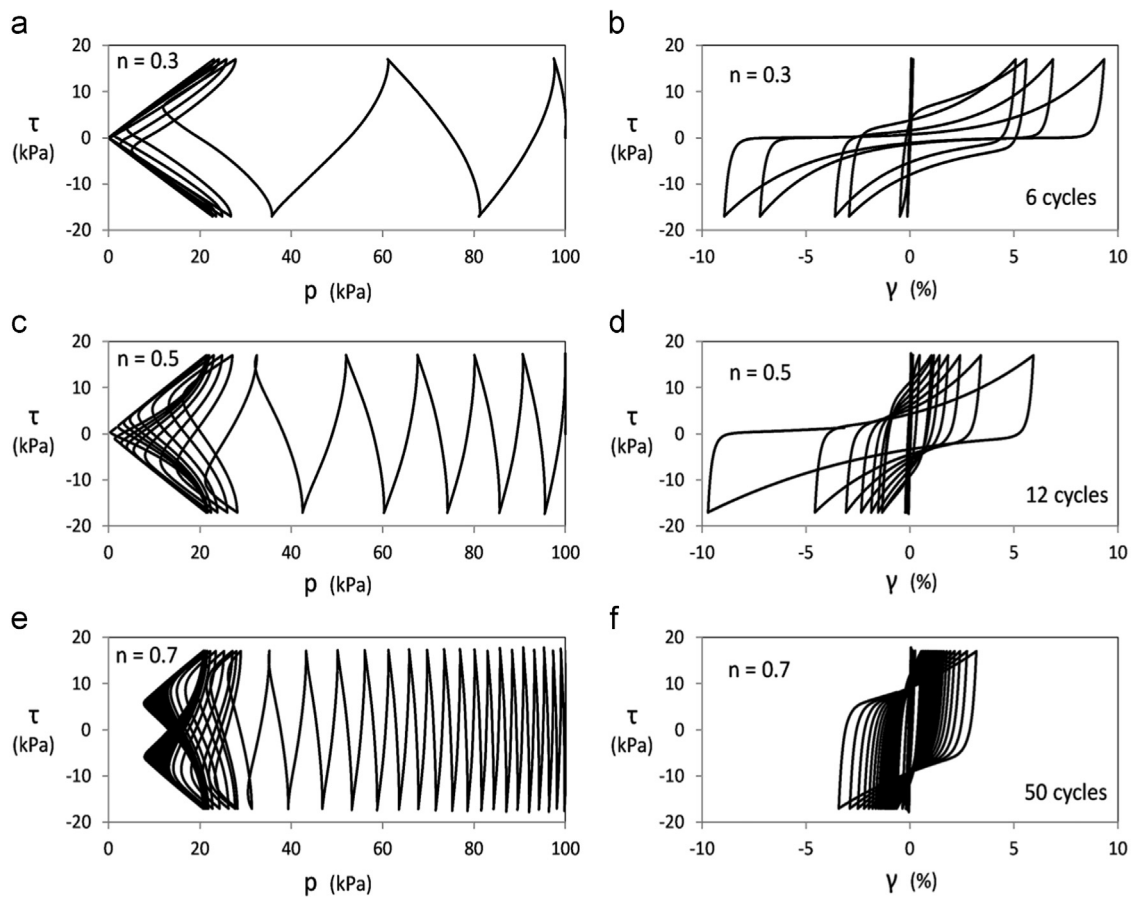


Fig. 8. Influence of exponent hardening parameter n on the simulated cyclic undrained response of sand.

3.4. Mapping rule and load reversal criterion

Update of the stress ratio tensor at pivot points, \mathbf{r}_p , in Eq. (16) occurs when the first order work changes sign; The first order work is equal to the inner product of the strain rate tensor and the difference of the current stress ratio tensor from the stress ratio tensor obtained by the last pivot point:

$$dW = (\mathbf{r} - \mathbf{r}_p) : \boldsymbol{\varepsilon} \quad (30)$$

Figs. 2–4 offer a schematic insight on how the shape of bounding surface, $f=0$, described by Eq. (16) is adjusted to the shape of the target failure surface [$F=0$ of Eq. (22)] for each stress path.

Initially, Fig. 2 illustrates certain snapshots of characteristic stress states in π -plane, corresponding to certain points in a stress–strain loop obtained by a cyclic simple shear test under constant mean effective stress. The resulting stress path is a straight line along $\theta=\pi/6$. The shapes of bounding, target failure and loading surfaces, $f=0$, $F=0$ and $L=0$, described by Eqs. (16), (22), and (24) respectively, are plotted in the π -plane plots along with the current stress point (star symbol). The beginning of loading corresponds to stress point A which lies on the hydrostatic axis ($\zeta=0$); therefore, the loading surface ($L=0$) collapses to a single line containing stress point A. From A to C–, the loading surface swells isotropically as ζ increases, until it coincides both with the target failure surface ($F=0$) for $\zeta=1$ (point E–) and the bounding surface ($f=0$), since \mathbf{r}_p is still equal to 0. At pivot point C+, the first order work, dW , changes sign, confirming the occurrence of loading reversal and \mathbf{r}_p obtains the values of point C–. At this moment, the loading surface trivializes once more to a

single point ($\zeta=0$), while the bounding surface, though convex in general, fits perfectly to the target failure surface at the point opposite to the current one (namely the “image” point). The “image” point always corresponds to the point where the projection of current $\mathbf{r}-\mathbf{r}_p$, crosses the surface $f=0$, as depicted in Fig. 3.

In order to verify the unique adaptation of the bounding surface for each stress path, the same graphical illustration is adopted in Fig. 4 for the case of a cyclic triaxial p-constant test. From points A to C–, the image is similar to that of Fig. 2, besides the fact that the stress points lies on $\theta=0$ (compression). Upon first reversal, point C+, the loading surface becomes a single point in π -plane coinciding with the stress point, while the bounding surface adapts in a way that fits the target failure at $\theta=\pi/3$ (“image” point). Upon second reversal, namely point E–, the stress ratio tensor, \mathbf{r}_p , is updated once again, so that this time the bounding surface coincides with the target failure one at $\theta=0$ (next “image” point).

Overall, Eq. (16) describes a uniquely adaptable bounding surface to the target surface for each specific stress path. In mathematical terms, the target surface is the geometric locus of the “image” points derived from the bounding surface. Consequently, the mapping rule is automatically incorporated in parameter ζ -since its definition is based on a reformulation of Eq. (16), and thus, in the plastic matrix {H}.

3.5. Flow rule

The stress-dilatancy relationship, adopted by the model, is based on Rowe’s dilatancy theory [33]. The ratio of the plastic volumetric strain increment, $d\varepsilon_p^v$, over the plastic deviatoric strain increment, $d\varepsilon_p^d$,

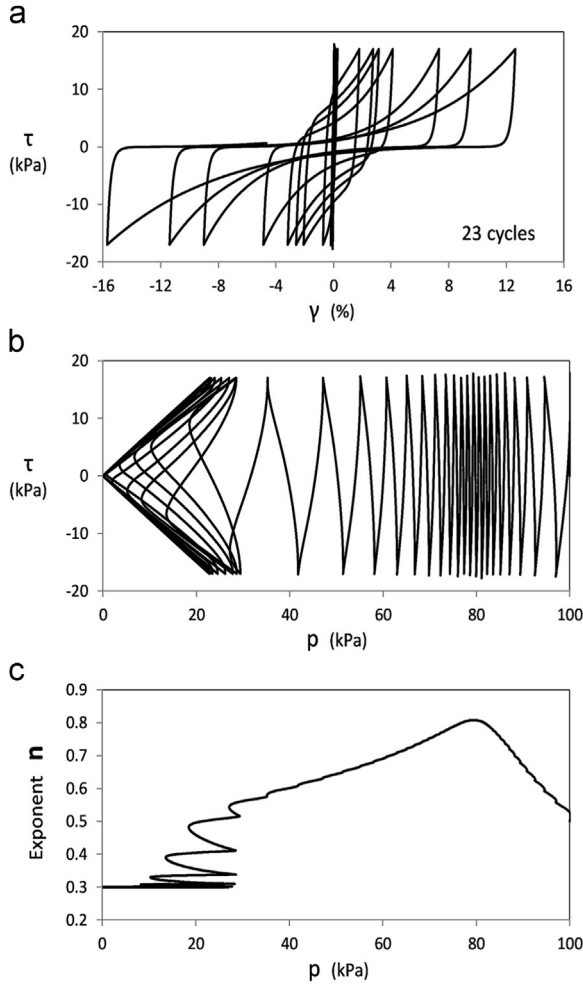


Fig. 9. Computed cyclic simple shear undrained response of a sand specimen with $D_r=70\%$. depends on the distance of the current stress ratio, q/p , in conventional p - q space from the phase transformation line, M_{pt} , as follows:

$$d = \frac{d\varepsilon_p^p}{d\varepsilon_q^p} = \left(M_{pt} - \frac{q}{p} \right) \quad (31)$$

When $q/p > M_{pt}$, the imposed deviatoric strain increment causes $d\varepsilon_p^p < 0$ and $d < 0$ which corresponds to dilation. Vice versa, when $q/p < M_{pt}$, $d\varepsilon_p^p > 0$ and $d > 0$ resulting in contraction. The dilatancy strain ratio, d , remains a scalar quantity in multiaxial stress-strain space, calculated by:

$$d = R_d \left(\sqrt{\frac{2}{3}} M_{pt} \chi \mathbf{n} - \frac{\mathbf{s}}{p} \right) : \mathbf{n} = R_d \left(\sqrt{\frac{2}{3}} M_{pt} \chi - \frac{\mathbf{s}}{p} : \mathbf{n} \right) \quad (32)$$

where χ is the factor described by Eq. (29) to account for the Lode angle effect and R_d is a parameter dependent on the current relative density which allows to capture densification effects due to cyclic drained loading.

The gradient to the plastic potential surface, necessary for the formation of the elastoplastic matrix of Eq. (10), is given by:

$$\Phi_g = \frac{\partial g}{\partial \boldsymbol{\sigma}} = \mathbf{n} + \mathbf{n}^2 d \quad (33)$$

Both volumetric and deviatoric nonassociativeness is applied. Dilatancy, d , is distributed to three plastic normal strain increments anisotropically, depending on the loading direction, which is represented by the normalized tensor \mathbf{n} . The increment of the plastic strain tensor can be obtained by Eq. (2). Due to the property of tensor \mathbf{n} , described by Eq. (21), the plastic volumetric increment,

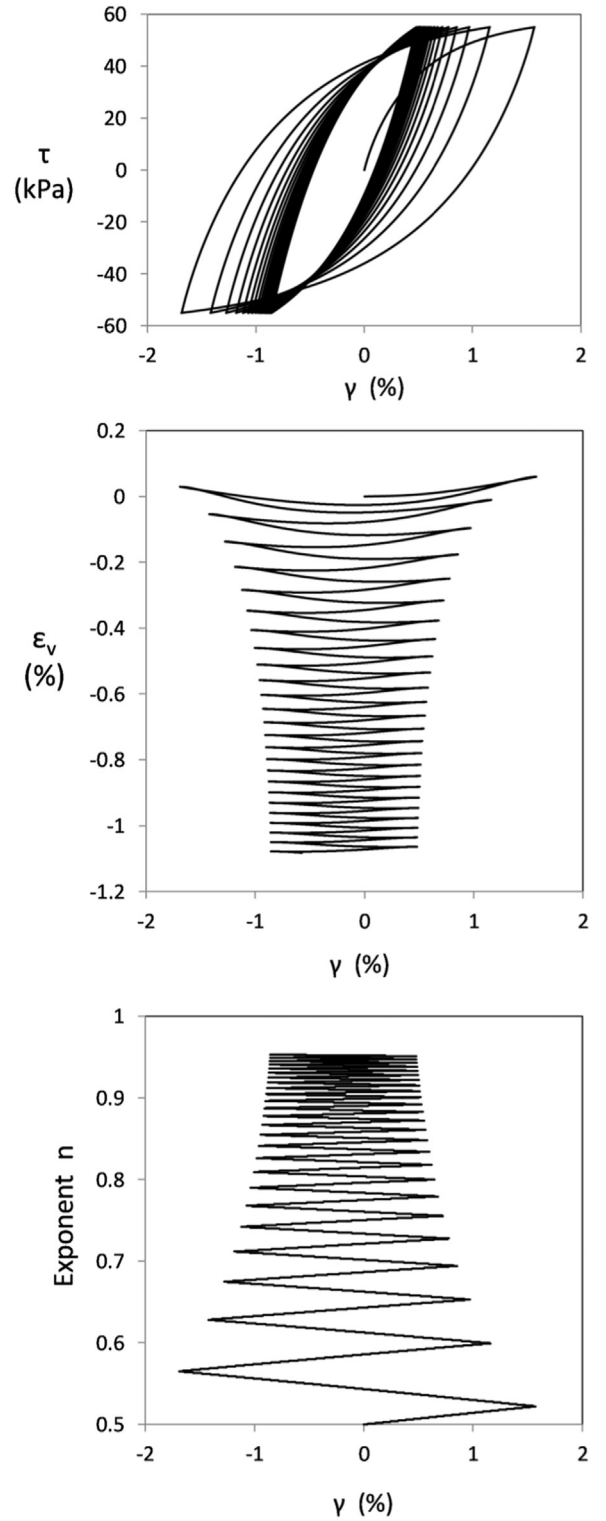


Fig. 10. Demonstration of drained cyclic simple shear response of a sand specimen with $D_{r0}=40\%$ under constant shear stress amplitude and evolving exponent n .

$d\varepsilon_p^p$, is indeed equal to:

$$\text{tr}(d\varepsilon_p^p) = \langle l \rangle \text{tr} \Phi_g = \langle l \rangle \text{tr} \mathbf{n}^2 = \langle l \rangle d \quad (34)$$

Thus far, it is common in literature (e.g. [5,7,9,27,28]) to arbitrarily assume an isotropic distribution of the quantity, d , to the three normal plastic strain increments, as indicated by the factor

Table 1
Model parameters and values for monotonic loading of Toyoura sand.

	FORMULATION A, Eqs (40)–(41)		FORMULATION B, Eq. (38)	
	Parameter	Values	Parameter	Values
Elasticity	A_o	130	A_o	130
	ν	0.15	ν	0.15
	m	0.8	m	0.8
Critical State	M_{cs}	1.25	M_{cs}	1.25
	–	–	e_o	0.934
	–	–	λ	0.019
	–	–	ξ	0.7
Bounding Surface & Dilatancy	Q	9.1	n_b	0.9
	R	0.75	n_d	0.7
	c	10	–	–
Hardening Exponent	n	0.35	n	0.25

1/3 in the following equation:

$$\Phi_g = \frac{\partial g}{\partial \sigma} = \mathbf{n} + \frac{d}{3}\mathbf{1} \quad (35)$$

This assumption finds its origin in the undrained behavior of fully saturated sand specimens and it is basically formed as such: Any tendency for volume change is equally attributed to the three normal components due to water incompressibility, irrespective of the type of loading. Although this is a reasonable assumption for undrained conditions, its validity is questioned in case of full drainage. Why equal tendency for normal deformation should be assumed in all three directions, when, for example, shear stress is only applied in one direction? In other words, why the out-of-plane plastic strain increment should be equal with the in-plane ones? To account for the effect of the loading direction on the distribution of the dilatancy, d , to the three normal plastic strain components, Eq. (33) is adopted. Comparison is held between Eqs. (33) and (35) in order to highlight the difference in stress and strain components.

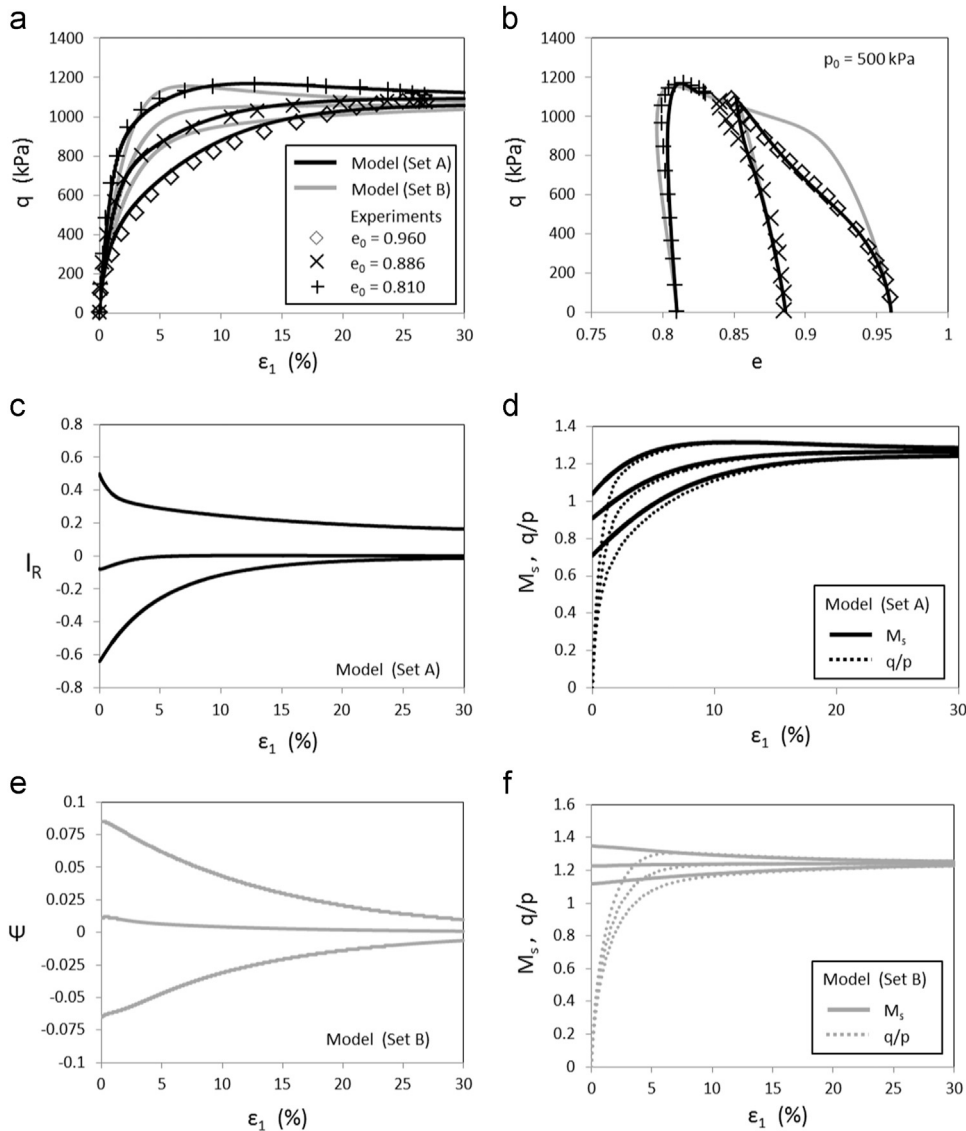


Fig. 11. (a), (b) Comparison between experimental data from monotonic drained triaxial tests on Toyoura sand with $p_o=100$ kPa [40] and model predictions using: i) formulation A [set of Eqs. (40–41)] and ii) formulation B [set of Eqs. (38)] for the bounding, M_s , and phase transformation stress ratios, M_{pt} (c), (d) Evolution of state variable, I_R , bounding stress ratio, M_s and stress ratio, q/p , versus axial strain for formulation A. (e), (f) Evolution of state variable, ψ , bounding stress ratio, M_s and stress ratio, q/p , versus axial strain for formulation B.

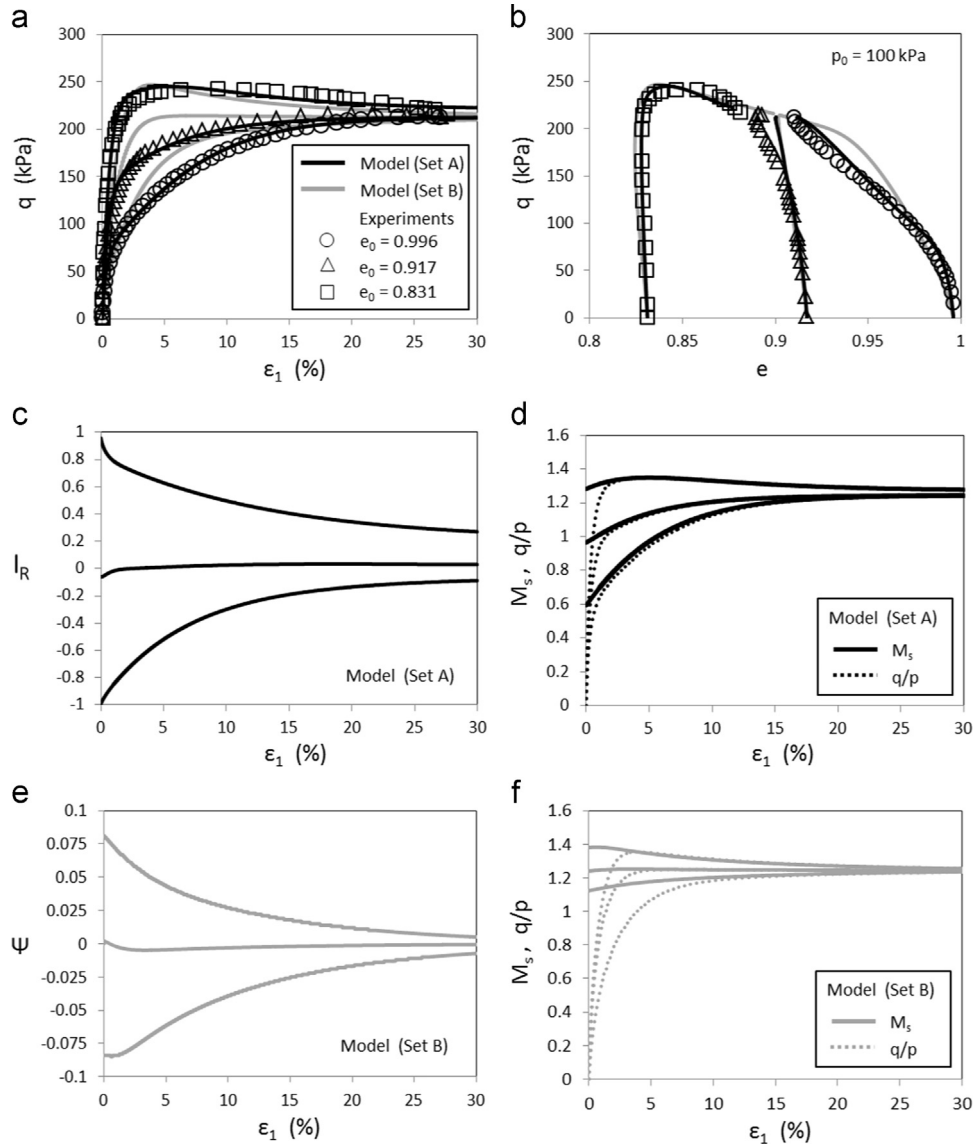


Fig. 12. (a), (b) Comparison between experimental data from monotonic drained triaxial tests on Toyoura sand with $p_0=100$ kPa [40] and model predictions using: i) formulation A [set of Eqs. (40–41)] and ii) formulation B [set of Eqs. (38)] for the bounding, M_s , and phase transformation stress ratios, M_{pt} . (c), (d) Evolution of state variable, I_R , bounding stress ratio, M_s and stress ratio, q/p , versus axial strain for formulation A. (e), (f) Evolution of state variable, ψ , bounding stress ratio, M_s and stress ratio, q/p , versus axial strain for formulation B.

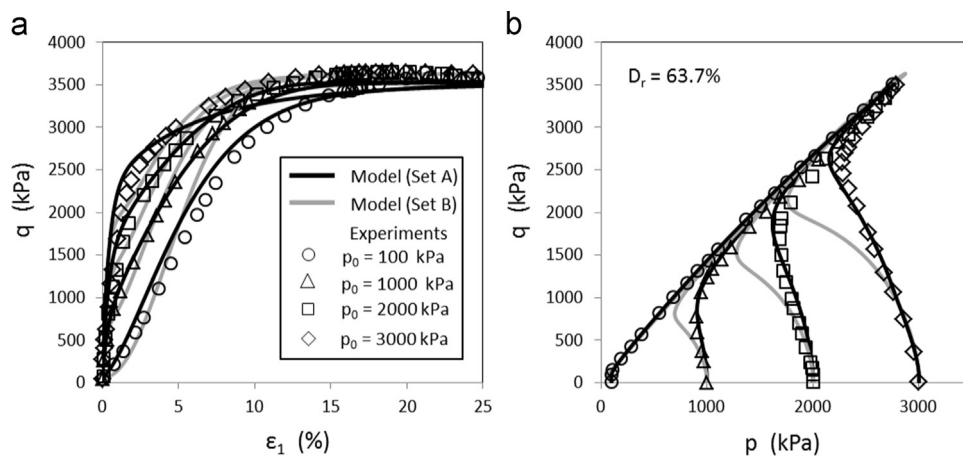


Fig. 13. Comparison between experimental data from monotonic undrained triaxial tests on Toyoura sand [40] and model predictions using: i) formulation A [set of Eqs. (40–41)] and ii) formulation B [set of Eqs. (38)] for the bounding, M_s , and phase transformation stress ratios, M_{pt} .

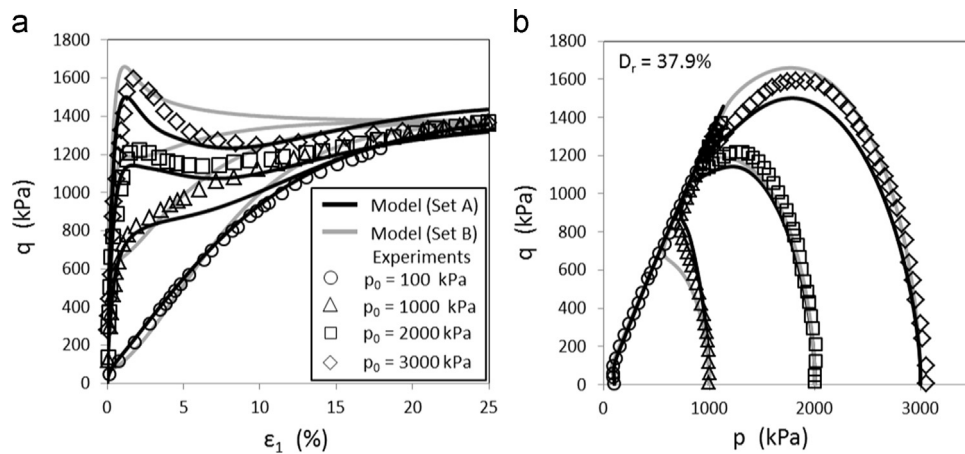


Fig. 14. Comparison between experimental data from monotonic undrained triaxial tests on Toyoura sand [40] and model predictions using: i) formulation A [set of Eqs. (40–41)] and ii) formulation B [set of Eqs. (38)] for the bounding, M_s and phase transformation stress ratios, M_{pt} .

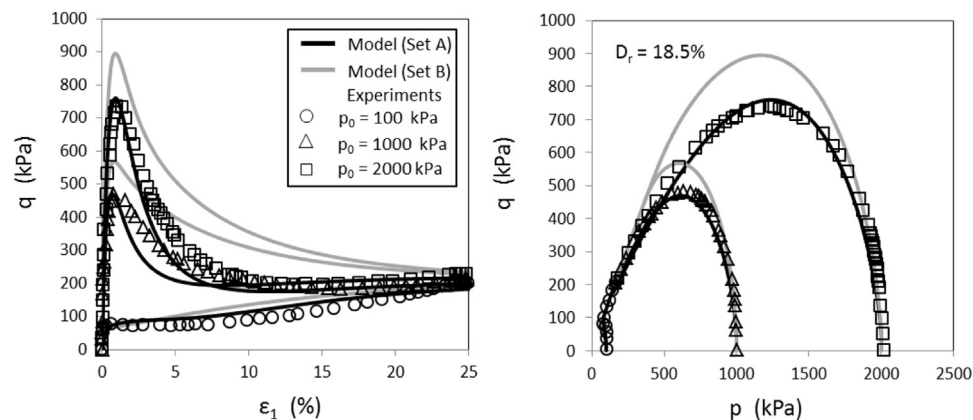


Fig. 15. Comparison between experimental data from monotonic undrained triaxial tests on Toyoura sand [40] and model predictions using: i) formulation A [set of Eqs. (40–41)] and ii) formulation B [set of Eqs. (38)] for the bounding, M_s and phase transformation stress ratios, M_{pt} .

Fig. 5 illustrates the distribution of normal strain components for a monotonic simple shear test, where only shear stress, σ_{12} , is applied. In terms of shear stress–strain curve the response is the same for both equations. Eq. (35) results in equal normal strains in all directions ($\epsilon_{ii} = \epsilon_p/3$), whereas Eq. (33) develops normal strains only in the directions related with the applied shear stress; ϵ_{11} and ϵ_{22} . The out of plane normal strain ϵ_{33} is zero, indicating that there is no tendency for contraction or dilation in the direction where no shear stress is applied.

In the case of an undrained cyclic simple shear test, where no normal strain is allowed and only σ_{12} is applied, the variation of normal stresses is identical when Eq. (35) is adopted, resulting in a path always lying on $\pi/6$ in π -plane plot, as depicted in Fig. 6. Alternatively, when Eq. (33) is used, the out of plane normal stress, σ_{33} , decreases in a slower rate during loading, resulting in a more complicated path as plotted in a π -plane graph. Whether Eqs. (33) or (35) is closer to reality is difficult to be documented, since elaborate experimental data are needed involving the measurement of each strain or stress component for a variety of stress paths.

Parameter R_d in Eq. (32) is given by:

$$R_d = e^{-\alpha(D_r - D_{r0})} \quad (36)$$

where D_r is the current relative density, D_{r0} is the initial relative density and α is a constant. Evidently, increase of D_r causes decrease of parameter R_d and subsequent decrease of quantity, d , resulting in densification as shown in Fig. 7 for the case of a drained cyclic simple shear element test. Parameter R_d is deliberately chosen as a function of D_r , so that R_d remains unity during

undrained loading. The calibration of constant α for the demonstration of Fig. 7 was based on the empirical correlations of volumetric strains with the number of cycles for 1% shear strain and $D_{r0} = 45\%$ [12,35].

3.6. Influence of hardening exponent n

Typical values of hardening exponent n for soils are found in the range of 0.2–0.8, as suggested by [11]. In general, the monotonic response is not extremely sensitive to hardening exponent n ; thus, a satisfactory prediction can be achieved with a specific value within the range of 0.2–0.5, for both drained and undrained conditions, accompanied by a proper calibration of the other model parameters. The same applies also for cyclic drained loading. However, the response under cyclic undrained loading is greatly affected by the value of n , especially in terms of number of cycles required to cause liquefaction ($p=0$), as shown in Fig. 8. Three different values of n have been used in an attempt to predict the response of a sand specimen with $D_{r0} = 70\%$ under simple shear undrained loading. In case of $n=0.3$, only 6 cycles of loading are required for liquefaction occurrence ($p=0$), while large shear strains $> 3\%$ develop abruptly after the 3rd cycle. As n increases (e.g. $n=0.5$), the required number of cycles also increases, until $n=0.7$ for which liquefaction cannot be practically achieved within a reasonable number of cycles. However, no strain locking is observed, and accumulation of shear strains continues with increasing loading cycles even for large values of n .

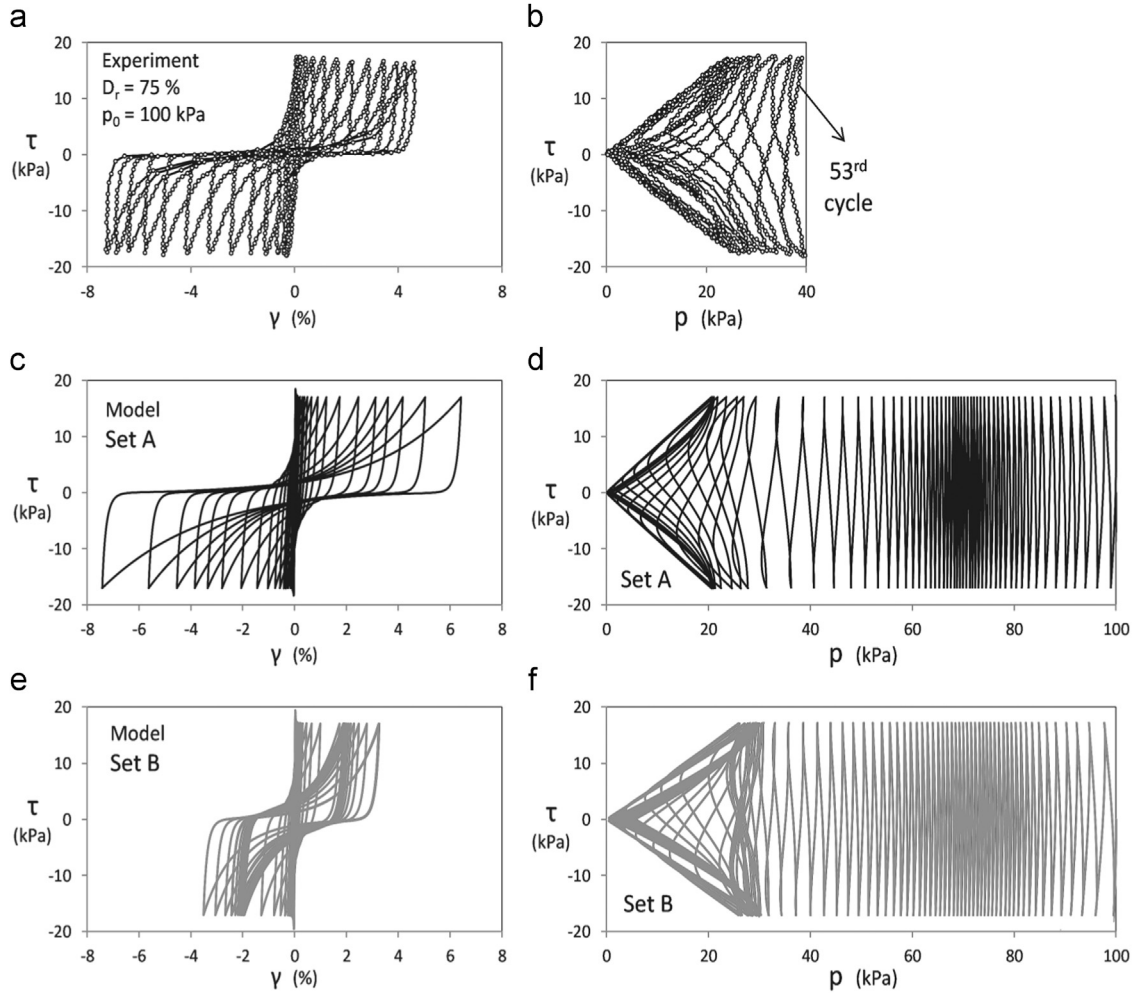


Fig. 16. Comparison between experimental data from cyclic undrained torsional shear tests on Toyoura sand [43] and model predictions using: i) formulation A [set of Eqs. (40–41)] and ii) formulation B [set of Eqs. (38)] for the bounding, M_s and phase transformation stress ratios, M_{pt} .

Exponent n is the crucial parameter to determine the number of cycles required to cause liquefaction, whether the criterion is $p=0$ or the shear strain exceeds a certain threshold (e.g. 3%). For more realistic results, similar to experimentally observed behavior, n is expressed as a function of the cumulative deviatoric strain increment:

$$n = n_f + \left[n_{\text{peak}} + (n_0 - n_{\text{peak}}) e^{-\beta \sum d\epsilon_q} - n_f \right] e^{-\gamma (1 - \text{sign}(\sum |d\epsilon_p|)) \sum d\epsilon_q} \quad (37)$$

In Eq. (37), n_f is the final desired value (when p tends to zero), n_0 is the initial value, n_{peak} is the potentially reached peak value dependent on constants β and γ . The rightmost exponential term of Eq. (37) depends on the function $1 - \text{sign}(\sum |d\epsilon_p|)$, where $\sum |d\epsilon_p|$ is the accumulation of volumetric strain increments. Undrained conditions impose that $d\epsilon_p = 0$; thus this function returns unity for undrained cyclic loading.

The resultant prediction by Eq. (37) is depicted in Fig. 9. A characteristic more rapid decrease of p is observed in the first two cycles ($n=0.5$), followed by slower decrease (for $n > 0.6$) until the rate of p reduction increases again so that liquefaction is achieved ($0.3 \leq n \leq 0.5$). In terms of stress–strain loops, there is a gradual increase of shear strain amplitude for each additional cycle.

Cyclic loading under drained conditions causes densification. When constant stress amplitude cycles of loading are applied, densification is reflected in the stress–strain loops through a gradual increase of the secant shear modulus and narrowing of the

loop (cyclic hardening). This behavior can be reproduced by continuously increasing the value of parameter n during loading. For this purpose, Eq. (37) is used, which, in case of drained loading, the last exponential at the right-hand side is deactivated, since $\sum |d\epsilon_p| > 0$, so that the function $1 - \text{sign}(\sum |d\epsilon_p|)$ becomes equal to zero. Demonstration of the impact of Eq. (37) on the predicted response is shown in Fig. 10.

3.7. Evolution of bounding and phase transformation stress ratios

3.7.1. Adopting the critical state concept

The essence of the critical state concept is that no change in volume occurs when the current stress state reaches the critical state despite the continuous increase of shear strain. In order to achieve this kind of performance upon critical state, both the phase transformation,¹ M_{pt} and the bounding stress ratios, M_s , should gradually converge to the critical state stress ratio, M_{cs} , producing zero plastic volumetric change when the stress ratio becomes equal to $M_s = M_{pt} = M_{cs}$, according to the flow rule of Eq. (31). Several suggestions have been made in literature for the

¹ Phase transformation stress ratio is referred to as dilatancy stress ratio by many researchers (e.g. [5,9,27,37]). However, in this paper the term “phase transformation stress ratio” is preferred, which was introduced by Ishihara et al., [21] after experimental observations and was adopted by many researchers on the field of constitutive modeling (e.g. [14,26]). It is believed by the authors to provide a more accurate description of the physical mechanism at hand.

Table 2
Model parameters and values for undrained cyclic loading of Toyoura sand.

	FORMULATION A, Eqs. (40)–(41)		FORMULATION B, Eqs. (38)	
	Parameter	Values	Parameter	Values
Elasticity	A_o	130	A_o	130
	ν	0.15	ν	0.15
	m	0.8	m	0.8
Critical state	M_{cs}	1.33	M_{cs}	1.33
	–	–	e_o	0.934
	–	–	λ	0.019
	–	–	ξ	0.7
Bounding surface & dilatancy	Q	9.1	n_b	0.9
	R	0.77	n_d	0.7
	c	4	–	–
Hardening exponent	n_o	0.5	n_o	1
n	n_f	0.3	n_f	0.2
	n_{peak}	8	n_{peak}	4.7
	β	3.5	β	105
	γ	30	γ	42

variation of M_s and M_{pt} , based on a suitable current state material parameter relative to the critical state [27,42]; one of the most recent and physically perceptible, being proposed by [9] and adopted also by [37]:

$$M_s = M_{cs} e^{-n_b \Psi} \quad \text{and} \quad M_{pt} = M_{cs} e^{n_d \Psi} \quad (38)$$

in which $\Psi = e - e_c$, e_c is the void ratio given by the critical state line in $e-p$ space described by:

$$e_c = e_o - \lambda \left(\frac{p}{p_{at}} \right)^\xi \quad (39)$$

and n_b , n_d positive material constants. The effectiveness of Eqs. (38) relies on three satisfied postulates: (i) when $e = e_c$ then $M_{pt} = M_s = M_{cs}$, (ii) for denser sands where $e < e_c$, then $M_{pt} < M_{cs} < M_s$ leading to dilatant response and (iii) for looser sands where $e > e_c$, then $M_{pt} < M_{cs} < M_s$ resulting in contraction. Although the above formulation [Eqs. (38)] works efficiently, at least for monotonic loading, the calibration process can be challenging should the measured behavior be reproduced for a wide variety of stress paths without readjusting n_b , n_d for each specific simulation.

Moreover, the above mentioned postulates are not necessarily satisfied in case of cyclic loading. For example, in case of cyclic mobility it has been experimentally observed [13,2,24,43,10] that cyclic loading moves the stress paths towards the critical state line in $q-p$ space which coincides with the so-called failure envelope at $p=0$. However, the state parameter Ψ cannot become equal to zero under cyclic strain accumulation, so that M_s converges eventually to M_{cs} . Therefore, Eqs. (38) lead to early stabilization at $p > 0$, hindering liquefaction occurrence and subsequent development of large strains [9]. As a result, extra features usually need to be added in a formulation, which are usually attributed to fabric-related effects (e.g. fabric-dilatancy tensor), as indicated by Dafalias and Manzari [9]. However, this modification may only contribute to a further decrease of p towards zero, but fails to reproduce the associated increase in shear strain amplitude. Indeed, M_s and M_{pt} still cannot converge to M_{cs} and shear locking cannot be eventually avoided.

After meticulous observation of experimental data and careful consideration of the above, an alternate formulation for the evolution of the bounding stress ratio was chosen as a function of the cumulative deviatoric strain increments, $\sum d\epsilon_q$:

$$M_s = M_{cs} + \left[M_{sp} + (M_{s0} - M_{sp}) e^{-c \sum d\epsilon_q} - M_{cs} \right] e^{-c \sum d\epsilon_q} \quad (40)$$

where M_{s0} is an initial value and M_{sp} is a maximum value that can be potentially reached depending on the model parameter c . For typical values of c in the range of 3–10, M_{sp} can never be reached. Instead, a lower value is reached, herein called M_{speak} .

The phase transformation stress ratio evolves in the same context, according to the following expression:

$$M_{pt} = M_{cs} + (M_{pt0} - M_{cs}) e^{-0.5c \sum d\epsilon_q} \quad (41)$$

where M_{pt0} is the initial value of M_{pt} . The use of cumulative deviatoric strain increments, $\sum d\epsilon_q$ ensures that critical state will be reached under monotonic and cyclic loading [38].

3.7.2. Using relative dilatancy index as state parameter

The proposed set of Eqs. (40) and (41) may present a more convenient and flexible formulation, but it lacks a parameter related to the critical state, that will provide a physical meaning. The latter can be achieved by correlating the model parameters M_{s0} , M_{sp} and M_{pt0} with Bolton's relative dilatancy index [3,6]:

$$I_R = D_r(Q - \ln(p)) - R \quad (42)$$

where D_r is the current relative density of the sand, p is the current mean effective stress, and Q , R are constants obtaining values close to 10 and 1, respectively. Critical state occurs when $I_R = 0$, while $I_R > 0$ indicates denser states of sands and $I_R < 0$ accounts for looser contractive states. For triaxial compression the maximum friction angle is given by Bolton [3], $\varphi_{max} - \varphi_{cs} = 3I_R$, thus:

$$M_{speak} = \frac{6 \sin(\varphi_{max})}{3 - \sin(\varphi_{max})} \quad (43)$$

The bounding stress ratio obtains its maximum value, M_{speak} , when:

$$\frac{\partial M_s}{\partial (\sum d\epsilon_q)} = 0 \Leftrightarrow \left(\sum d\epsilon_q \right)_{peak} = \frac{1}{c} \ln \left(\frac{M_{cs} - M_{sp}}{2(M_{s0} - M_{sp})} \right) \quad (44)$$

where the initial value, M_{s0} , is given by:

$$M_{s0} = \frac{6 \sin(0.8\varphi_{cs} + 3I_{R0})}{3 - \sin(0.8\varphi_{cs} + 3I_{R0})} \quad (45)$$

with I_{R0} being the initial value of the relative dilatancy index, I_R . Substituting Eq. (44) to Eq. (40), M_{sp} is obtained:

$$M_{sp} = 2M_{speak} - M_{cs} + 0.5 \sqrt{(2M_{cs} - 4M_{speak})^2 - 16M_{s0}(M_{speak} - M_{cs}) + 4M_{cs}^2} \quad (46)$$

After statistical processing of numerous drained tests on sands, Bolton [3] suggested that:

$$\left[-\frac{d\epsilon_p}{d\epsilon_1} \right]_{max} = 0.3I_R \quad (47)$$

when the peak strength value, M_{speak} , is reached; a deduction that can be used for the calibration of the plastic flow rule and specifically, the phase transformation stress ratio. Combining Eqs. (31) and (47) for triaxial loading test conditions ($d\epsilon_2 = d\epsilon_3$), assuming that $\left[\frac{d\epsilon_p}{d\epsilon_q} \right]_{max} \approx \left[\frac{d\epsilon_p}{d\epsilon_q} \right]_{max}$ when maximum strength ($\zeta = 1$)

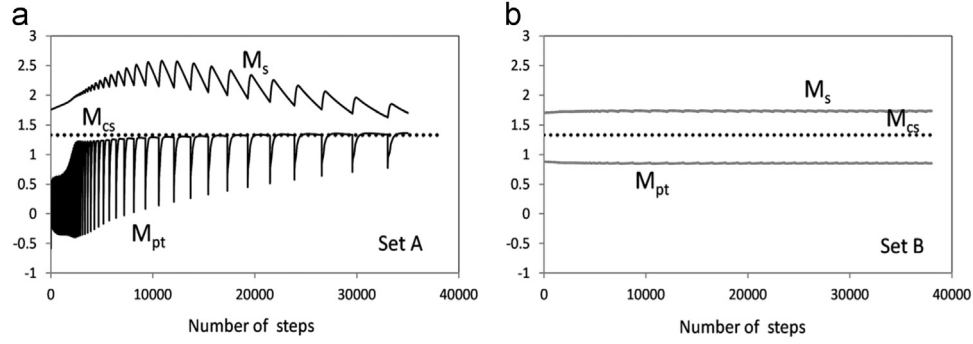


Fig. 17. Evolution of bounding, M_s and phase transformation stress ratios, M_{pt} for model prediction of experimental data from cyclic undrained torsional shear tests on Toyoura sand [43] of Fig. 15 using: i) formulation A [set of Eqs. (40–41)] and ii) formulation B [set of Eqs. (38)].

occurs, it is shown that:

$$\left[\frac{d\epsilon_p^p}{d\epsilon_q^p} \right]_{\max,tx} = M_{pt,peak} - M_{speak} = \frac{-3 \left[-\frac{d\epsilon_p}{d\epsilon_1} \right]_{\max}}{3 + \left[-\frac{d\epsilon_p}{d\epsilon_1} \right]_{\max}} = \frac{-3(0.3I_R)}{3 + (0.3I_R)} \quad (48)$$

In order to satisfy the above requirement [Eq. (48)], M_{pto} is deliberately chosen as:

$$M_{pto} = M_s \zeta^n - \frac{3(0.3I_R)}{3 - 3(0.3I_R)} \quad (49)$$

so that, according to Eq. (41), $M_{pt} \approx M_{pto} = M_{speak} - \frac{3(0.3I_R)}{3 - 3(0.3I_R)}$ at peak strength ($\zeta = 1$).

In retrospect, by following the above described calibration process, the initially “physically meaningless” model parameters M_{s0} , M_{sp} and M_{pto} are eventually expressed as functions of the fundamental soil properties φ_{cs} , D_r and current confining pressure p .

4. Model prediction versus experiments

Model predictions versus experimental results have been performed for both formulation of M_s and M_{pt} : formulation A [set of Eqs. (40–41)] and formulation B [set of Eqs. (38)] to evaluate the efficacy of the proposed formulation A compared to the well-established formulation B. Both formulations have been incorporated in the constitutive formulation proposed in this paper. Initially, simulations of drained and undrained triaxial monotonic tests for Toyoura sand were conducted. The values of the model parameters adopted in these simulations, are depicted in Table 1 for both formulations. The relative density, D_r , was calculated considering $e_{\max} = 0.977$ and $e_{\min} = 0.597$ for Toyoura sand, according to Verdugo and Ishihara [40]. Figs. 11–15(a) and (b) illustrate the comparison between model predictions and experiments. The flexibility offered by the proposed formulation for M_s and M_{pt} provides a better agreement with the experiments, especially for loose sands. In case of denser sands, the level of predictability can be considered equal for both models.

Figs. 11–12(c) and (d) offer an insight on how the new presented constitutive formulation cooperates with the two formulations for M_s and M_{pt} based on the evolution of state parameter I_R for formulation A and Ψ for formulation B. The required parameters for the critical state line in $e-p$ space, λ and ξ , were obtained from Taiebat and Dafalias [37]. The differences between the two formulations are mostly attributed to the initial values of M_s which in case of formulation A are lower than M_{cs} for both the looser and denser sand. According to these new equations, the stress ratio q/p reaches the bounding surface early during loading following its shape up to the critical state. On the other hand, for formulation B, the stress ratio meets the bounding surface later

during loading at a higher current value of M_s and then follows the bounding surface up to critical state in a much slower rate.

In the following, undrained cyclic loading was simulated and compared with experimental results, as depicted in Fig. 16. In order to efficiently capture the number of cycles to liquefaction, Eq. (37) was adopted. The values of the model parameters considered in the simulations are presented in Table 2, for both formulations. Evidently, model simulation incorporating formulation A, captures better the stress–strain loops. On the other hand, when formulation B is adopted, shear locking is observed despite the fact that early stabilization (at $p > 0$) is avoided, and liquefaction ($p = 0$) eventually occurs. This is accomplished without the use of a fabric-related parameter as it has been applied by Dafalias and Manzari [9] in the framework of classical bounding elastoplasticity); an achievement attributed to the proposed plasticity approach. To elucidate the differences between the two formulations, Fig. 17 plots the evolution of M_s and M_{pt} with the number of strain increments (steps). In case of formulation B, M_s and M_{pt} , despite the negligible fluctuations due to variation of Ψ , are practically constants throughout loading, far from their critical state value; a fact which eventually leads to shear locking. On the other hand, formulation A leads to a continuous variation of both M_s and M_{pt} that tend to an asymptotic oscillatory convergence to M_{cs} (due to significant variation of I_R). Overall, formulation A [Eqs. (40–41)] offers a higher degree of versatility and flexibility allowing for more consistent predictions of sand behavior under monotonic or cyclic loading; thus it is adopted by the proposed constitutive model.

5. Summary

A new plasticity framework for sand behavior in multiaxial stress–strain space is developed by combining perfect plasticity with components of smooth hysteretic modeling of the Bouc–Wen type. The proposed formulation incorporates many innovations (such as new mapping and plastic flow rules) intended to provide critical state compatibility not only for monotonic but also for cyclic loading and uniqueness of model parameters for a given type of sand. The comparison with experimental results reveals the capability of the model to describe complex patterns of sand behavior as well as its flexibility to predict liquefaction and cyclic mobility, developing very large strains (e.g. $\gamma > 8\%$) without exhibiting shear locking. This very important feature is mainly attributed to a new formulation for the evolution the bounding and phase transformation stress ratios that ensures asymptotic convergence to critical state for all types of applied loading. Implementation of the Ta-Ger sand model in a commercially available finite element analysis program is currently under development and appears promising.

Acknowledgments

This research has been co-financed by the European Union (European Social Fund – ESF) and Greek national funds through the Operational Program "Education and Lifelong Learning" of the National Strategic Reference Framework (NSRF)-Research Funding Program: Thales. Investing in knowledge society through the European Social Fund, Project ID "UPGRADE".

Appendix

Elasticity matrix:

$$E^e = \begin{bmatrix} E_1 & E_2 & E_2 & 0 & 0 & 0 \\ E_2 & E_1 & E_2 & 0 & 0 & 0 \\ E_2 & E_2 & E_1 & 0 & 0 & 0 \\ 0 & 0 & 0 & 2G & 0 & 0 \\ 0 & 0 & 0 & 0 & 2G & 0 \\ 0 & 0 & 0 & 0 & 0 & 2G \end{bmatrix} \quad (I)$$

where:

$$E_1 = K + \frac{4G}{3} \quad (II)$$

and

$$E_2 = K - \frac{2G}{3} \quad (III)$$

in which, G and K are the elastic shear and bulk moduli, in respect.

Elasto-plastic Matrix E_h^{ep}

$$E_h^{ep} = \begin{bmatrix} A_1 & A_2 & A_3 & A_4 & A_5 & A_6 \\ B_1 & B_2 & B_3 & B_4 & B_5 & B_6 \\ C_1 & C_2 & C_3 & C_4 & C_5 & C_6 \\ D_1 & D_2 & D_3 & D_4 & D_5 & D_6 \\ E_1 & E_2 & E_3 & E_4 & E_5 & E_6 \\ F_1 & F_2 & F_3 & F_4 & F_5 & F_6 \end{bmatrix} \quad (IV)$$

$$\begin{bmatrix} d\sigma_{11} \\ d\sigma_{22} \\ d\sigma_{33} \\ d\sigma_{12} \\ d\sigma_{23} \\ d\sigma_{31} \end{bmatrix} = \begin{bmatrix} A_1 & A_2 & A_3 & A_4 & A_5 & A_6 \\ B_1 & B_2 & B_3 & B_4 & B_5 & B_6 \\ C_1 & C_2 & C_3 & C_4 & C_5 & C_6 \\ D_1 & D_2 & D_3 & D_4 & D_5 & D_6 \\ E_1 & E_2 & E_3 & E_4 & E_5 & E_6 \\ F_1 & F_2 & F_3 & F_4 & F_5 & F_6 \end{bmatrix} \begin{bmatrix} d\varepsilon_{11} \\ d\varepsilon_{22} \\ d\varepsilon_{33} \\ d\varepsilon_{12} \\ d\varepsilon_{23} \\ d\varepsilon_{31} \end{bmatrix} \quad (V)$$

The components of the elastoplastic matrix are given by:

$$\begin{aligned} A_1 &= E_1 - \frac{\zeta^n}{S} (\Phi_{f,11}E_1 + \Phi_{f,22}E_2 + \Phi_{f,33}E_2) (\Phi_{g,11}E_1 + \Phi_{g,22}E_2 + \Phi_{g,33}E_2) \\ A_2 &= E_2 - \frac{\zeta^n}{S} (\Phi_{f,11}E_2 + \Phi_{f,22}E_1 + \Phi_{f,33}E_2) (\Phi_{g,11}E_1 + \Phi_{g,22}E_2 + \Phi_{g,33}E_2) \\ A_3 &= E_2 - \frac{\zeta^n}{S} (\Phi_{f,11}E_2 + \Phi_{f,22}E_2 + \Phi_{f,33}E_1) (\Phi_{g,11}E_1 + \Phi_{g,22}E_2 + \Phi_{g,33}E_2) \\ A_4 &= -\frac{2G\zeta^n}{S} (\Phi_{g,11}E_1 + \Phi_{g,22}E_2 + \Phi_{g,33}E_2) \Phi_{f,12} \\ A_5 &= -\frac{2G\zeta^n}{S} (\Phi_{g,11}E_1 + \Phi_{g,22}E_2 + \Phi_{g,33}E_2) \Phi_{f,23} \\ A_6 &= -\frac{2G\zeta^n}{S} (\Phi_{g,11}E_1 + \Phi_{g,22}E_2 + \Phi_{g,33}E_2) \Phi_{f,31} \end{aligned} \quad (VI)$$

$$\begin{aligned} B_1 &= E_2 - \frac{\zeta^n}{S} (\Phi_{f,11}E_1 + \Phi_{f,22}E_2 + \Phi_{f,33}E_2) (\Phi_{g,11}E_2 + \Phi_{g,22}E_1 + \Phi_{g,33}E_2) \\ B_2 &= E_2 - \frac{\zeta^n}{S} (\Phi_{f,11}E_2 + \Phi_{f,22}E_1 + \Phi_{f,33}E_2) (\Phi_{g,11}E_2 + \Phi_{g,22}E_1 + \Phi_{g,33}E_2) \\ B_3 &= E_2 - \frac{\zeta^n}{S} (\Phi_{f,11}E_2 + \Phi_{f,22}E_2 + \Phi_{f,33}E_1) (\Phi_{g,11}E_2 + \Phi_{g,22}E_1 + \Phi_{g,33}E_2) \\ B_4 &= -\frac{2G\zeta^n}{S} (\Phi_{g,11}E_2 + \Phi_{g,22}E_1 + \Phi_{g,33}E_2) \Phi_{f,12} \\ B_5 &= -\frac{2G\zeta^n}{S} (\Phi_{g,11}E_2 + \Phi_{g,22}E_1 + \Phi_{g,33}E_2) \Phi_{f,23} \\ B_6 &= -\frac{2G\zeta^n}{S} (\Phi_{g,11}E_2 + \Phi_{g,22}E_1 + \Phi_{g,33}E_2) \Phi_{f,31} \end{aligned} \quad (VII)$$

$$\begin{aligned} C_1 &= E_2 - \frac{\zeta^n}{S} (\Phi_{f,11}E_1 + \Phi_{f,22}E_2 + \Phi_{f,33}E_2) (\Phi_{g,11}E_2 + \Phi_{g,22}E_2 + \Phi_{g,33}E_1) \\ C_2 &= E_2 - \frac{\zeta^n}{S} (\Phi_{f,11}E_2 + \Phi_{f,22}E_1 + \Phi_{f,33}E_2) (\Phi_{g,11}E_2 + \Phi_{g,22}E_2 + \Phi_{g,33}E_1) \\ C_3 &= E_2 - \frac{\zeta^n}{S} (\Phi_{f,11}E_2 + \Phi_{f,22}E_2 + \Phi_{f,33}E_1) (\Phi_{g,11}E_2 + \Phi_{g,22}E_2 + \Phi_{g,33}E_1) \\ C_4 &= -\frac{2G\zeta^n}{S} (\Phi_{g,11}E_2 + \Phi_{g,22}E_2 + \Phi_{g,33}E_1) \Phi_{f,12} \\ C_5 &= -\frac{2G\zeta^n}{S} (\Phi_{g,11}E_2 + \Phi_{g,22}E_2 + \Phi_{g,33}E_1) \Phi_{f,23} \\ C_6 &= -\frac{2G\zeta^n}{S} (\Phi_{g,11}E_2 + \Phi_{g,22}E_2 + \Phi_{g,33}E_1) \Phi_{f,31} \end{aligned} \quad (VIII)$$

$$\begin{aligned} D_1 &= -\frac{2G\zeta^n}{S} (\Phi_{f,11}E_1 + \Phi_{f,22}E_2 + \Phi_{f,33}E_2) \Phi_{g,12} \\ D_2 &= -\frac{2G\zeta^n}{S} (\Phi_{f,11}E_2 + \Phi_{f,22}E_1 + \Phi_{f,33}E_2) \Phi_{g,12} \\ D_3 &= -\frac{2G\zeta^n}{S} (\Phi_{f,11}E_2 + \Phi_{f,22}E_2 + \Phi_{f,33}E_1) \Phi_{g,12} \\ D_4 &= 2G \left(1 - \frac{2G\zeta^n}{S} \Phi_{f,12} \Phi_{g,12} \right) \\ D_5 &= -\frac{4G^2\zeta^n}{S} \Phi_{f,12} \Phi_{g,23} \\ D_6 &= -\frac{4G^2\zeta^n}{S} \Phi_{f,12} \Phi_{g,31} \end{aligned} \quad (IX)$$

$$\begin{aligned} L_1 &= -\frac{2G\zeta^n}{S} (\Phi_{f,11}E_1 + \Phi_{f,22}E_2 + \Phi_{f,33}E_2) \Phi_{g,23} \\ L_2 &= -\frac{2G\zeta^n}{S} (\Phi_{f,11}E_2 + \Phi_{f,22}E_1 + \Phi_{f,33}E_2) \Phi_{g,23} \\ L_3 &= -\frac{2G\zeta^n}{S} (\Phi_{f,11}E_2 + \Phi_{f,22}E_2 + \Phi_{f,33}E_1) \Phi_{g,23} \\ L_4 &= -\frac{4G^2\zeta^n}{S} \Phi_{f,23} \Phi_{g,12} \\ L_5 &= 2G \left(1 - \frac{2G\zeta^n}{S} \Phi_{f,23} \Phi_{g,23} \right) \\ L_6 &= -\frac{4G^2\zeta^n}{S} \Phi_{f,23} \Phi_{g,31} \end{aligned} \quad (X)$$

$$\begin{aligned} F_1 &= -\frac{2G\zeta^n}{S} (\Phi_{f,11}E_1 + \Phi_{f,22}E_2 + \Phi_{f,33}E_2) \Phi_{g,31} \\ F_2 &= -\frac{2G\zeta^n}{S} (\Phi_{f,11}E_2 + \Phi_{f,22}E_1 + \Phi_{f,33}E_2) \Phi_{g,31} \\ F_3 &= -\frac{2G\zeta^n}{S} (\Phi_{f,11}E_2 + \Phi_{f,22}E_2 + \Phi_{f,33}E_1) \Phi_{g,31} \\ F_4 &= -\frac{4G^2\zeta^n}{S} \Phi_{f,31} \Phi_{g,12} \\ F_5 &= -\frac{4G^2\zeta^n}{S} \Phi_{f,31} \Phi_{g,23} \\ F_6 &= 2G \left(1 - \frac{2G\zeta^n}{S} \Phi_{f,31} \Phi_{g,31} \right) \end{aligned} \quad (XI)$$

where:

$$\begin{aligned} S &= \Phi_{g,11} (E_1 \Phi_{f,11} + E_2 \Phi_{f,22} + E_2 \Phi_{f,33}) \\ &+ \Phi_{g,22} (E_2 \Phi_{f,11} + E_1 \Phi_{f,22} + E_2 \Phi_{f,33}) \\ &+ \Phi_{g,33} (E_2 \Phi_{f,11} + E_2 \Phi_{f,22} + E_1 \Phi_{f,33}) + \\ &+ 2G (\Phi_{g,12} \Phi_{f,12}) + 2G (\Phi_{g,23} \Phi_{f,23}) + 2G (\Phi_{g,31} \Phi_{f,31}) \end{aligned} \quad (XII)$$

References

- [1] Been K, Jefferies MG. A state parameter for sands. *Geotechnique* 1985;35(2):99–112.
- [2] Been K, Jefferies MG. Soil liquefaction. A critical state approach. Taylor & Francis; 2006.
- [3] Bolton MD. The strength and dilatancy of sands. *Geotechnique* 1986;36(1):65–78.
- [4] Bouc R. Modele mathematique d' hysteresis. *Acustica* 1971;21:16–25.

- [5] Boulanger RW, Ziotopoulou K. Formulation of a sand plasticity plane-strain model for earthquake engineering applications. *Soil Dyn Earthq Eng* 2013;53:254–67.
- [6] Ching J, Chen JR, Yeh JY, Phoon KK. Updating uncertainties in friction angles of clean sands. *J Geotech Geoenviron Engineering*, 138, ASCE; 2012. p. 217–29.
- [7] Cubrinovski M, Ishihara K. State concept and modified elastoplasticity for sand modelling. *Soils Found* 2000;40(5):124–5.
- [8] Dafalias YF. Bounding surface plasticity. i: mathematical foundation and hypoplasticity. *J Eng Mech* 1986;112(9):966–87.
- [9] Dafalias YF, Manzari MT. Simple plasticity sand model accounting for fabric change effects. *J Eng Mech* 2004;130:622–34.
- [10] De Alba P, Seed HB, Chan CK. Sand liquefaction in large-scale simple shear tests. *J Soil Mech Found Div* 1976;102:909–27.
- [11] Drosos VA, Gerolymos N, Gazetas G. Constitutive model for soil amplification of ground shaking: Parameter calibration, comparisons, validation. *Soil Dyn Earthq Eng* 2012;42:255–74.
- [12] Duku PM, Stewart JP, Whang DH. Volumetric strains of clean sands subject to cyclic loads. *J Geotech Geoenviron Eng* 2008;134:1073–85.
- [13] Elgamal, AW, Dobry, R, Parra, E, Yang, Z. Soil dilation and shear deformation during liquefaction. In: Prakash S. (editor). Proceedings of the 4th international conference on case histories in geotechnical engineering, St Louis, Missouri, March 8–15; 1998. p. 22.
- [14] Elgamal A, Yang Z, Parra E. Computational modeling of cyclic mobility and post-liquefaction site response. *Soil Dyn Earthq Eng* 2002;22(4):259–71.
- [15] Gerolymos N, Gazetas G. Constitutive model for 1-D cyclic soil behavior applied to seismic analysis of layered deposits. *Soils Found* 2005;45(3):147–59.
- [16] Gerolymos N, Gazetas G, Vardoulakis I. A Thermo-poro-viscoplastic shear band model for seismic triggering and evolution of catastrophic landslides. *Soils Found* 2007;47(1):11–25.
- [17] Gerolymos N, Drosos V, Gazetas G. Seismic response of single-column bent on pile: evidence of beneficial role of pile and soil inelasticity. *Bull Earthq Eng* 2009;7(2):547–73.
- [18] Gerolymos N. Numerical modeling of seismic triggering, evolution, and deposition of rapid landslides: application to Higashi Takezawa (2004). *Int J Numer Anal Methods Geomech* 2010;34(4):383–407.
- [19] Gudehus G. A comprehensive constitutive equation for granular materials. *Soils Found* 1996;36(1):1–12.
- [20] Ishihara K. Soil behavior in earthquake geotechnics. New York: Oxford University Press; 1996.
- [21] Ishihara K, Tatsuoka F, Yasuda S. Undrained deformation and liquefaction of sand under cyclic stresses. *Soils Found* 1975;15(1):29–44.
- [22] Ishihara K, Towhata I. One-dimensional soil response analysis during earthquakes based on effective stress method. *J Fac Eng, Univ Tokyo (B)* 1980;35(4):665–700.
- [23] Kolymbas D. Barodesy: a new hypoplastic approach. *Int J Numer Anal Methods Geomech* 2012;36(9):1220–40.
- [24] Kramer SL. Geotechnical earthquake engineering. New Jersey: Prentice Hall, Inc.; 1996. p. 653.
- [25] Li XS, Dafalias YF. Dilatancy for cohesionless soils. *Géotechnique* 2000;50(4):449–60.
- [26] Li XS, Dafalias YF, Wang Z-L. State dependent dilatancy in critical state constitutive modelling of sand. *Can Geotech J* 1999;36:599–611.
- [27] Manzari MT, Dafalias YF. A two-surface critical plasticity model for sand. *Géotechnique* 1997;47(2):255–72.
- [28] Papadimitriou AG, Bouckovalas GD, Dafalias YF. Plasticity model for sand under small and large cyclic strains. *J Geotech Geoenviron Eng* 2001;127:973–83.
- [29] Park SS, Byrne PM. Practical constitutive model for soil liquefaction. In: Proceedings of the 9th international symposium on numerical models in geomechanics, Ottawa, Canada; 2004. pp. 181–186.
- [30] Pastor M, Zienkiewicz OC, Chan AHC. Generalized plasticity and the modelling of soil behaviour. *Int J Numer Anal Methods Geomech* 1990;14(3):151–90.
- [31] Prevost. JH. A simple plasticity theory for frictional cohesionless soils. *Soil Dyn Earthq Eng* 1985;4(1):9–17.
- [32] Richart Jr. FE, Hall JR, Woods RD. Vibration of soils and foundations. International series in theoretical and applied mechanics. Englewood Cliffs, N.J: Prentice-Hall; 1970.
- [33] Rowe PW. The stress-dilatancy relation for static equilibrium of an assembly of particles in contact. *Proc R Soc Lond Ser A* 1962;269:500–27.
- [34] Sivaselvan MV, Reinhorn AM. Hysteretic models for deteriorating inelastic structures. *J Eng Mech* 2000;126(6):633–40.
- [35] Silver ML, Seed HB. Volume changes in sand during cyclic loading. *J Soil Mech Found Div* 1971;9:1171–82.
- [36] Taborda DM, Zdravkovic L, Kontoe S, Potts DM. Computational study on the modification of a bounding surface plasticity model for sands. *Comput Geotech* 2014;59:145–60.
- [37] Taiebat M, Dafalias YF. SANISAND: Simple anisotropic sand plasticity model. *Int J Numer Anal Methods Geomech* 2007;32(8):915–48.
- [38] Tasiopoulou P, Gerolymos N. Development of a modified elastoplasticity model for sand. In: Proceedings of the second international conference on performance-based design in earthquake geotechnical engineering, Taormina (Italy), CD Rom, 28–30 May; 2012.
- [39] Triantafyllou S, Koumoussis V. An hysteretic quadrilateral plane stress element. *Arch Appl Mech* 2012;82:1675–87.
- [40] Verdugo R, Ishihara K. The steady state of sandy soils. *Soils Found* 1996;36(2):81–91.
- [41] Wen YK. Method for random vibration of hysteretic systems. *J Eng Mech* 1976;102:249–63.
- [42] Wood DM, Belkheir K, Liu DF. Strain softening and state parameter for sand modeling. *Géotechnique* 1994;44(2):335–9.
- [43] Zhang JM, Shamoto Y, Tokimatsu K. Moving critical and phase-transformation stress state lines of saturated sand during undrained cyclic shear. *Soils Found* 1997;37(2):51–9.